Applied Catalysis B: Environmental 325 (2023) 122367

Contents lists available at ScienceDirect

Applied Catalysis B: Environmental

journal homepage: www.elsevier.com/locate/apcatb

Collectively exhaustive electrochemical hydrogen evolution reaction of polymorphic cobalt selenides derived from organic surfactants modified Co-MOFs

Pitchai Thangasamy [a], Rong He [a], Hyacinthe Randriamahazaka [b], Xinqi Chen [c], Yizhi Zhang [d], Hongmei Luo [a], Haiyan Wang [d], Meng Zhou [a,*]

[a] Department of Chemical & Materials Engineering, New Mexico State University, Las Cruces, NM 88003, USA
[b] Université Paris Cité, CNRS, ITODYS, F-75006 Paris, France
[c] Northwestern University Atomic and Nanoscale Characterization Experimental (NUANCE) Center and Department of Materials Science and Engineering, Northwestern University, Evanston, IL 60208, USA
[d] School of Materials Engineering, Purdue University, West Lafayette, IN 47907, USA

ARTICLE INFO

Keywords:
Cobalt selenide
Co-MOF
Hydrogen evolution reaction
Activation energy
Volmer-Tafel pathway
Mechanistic investigation

ABSTRACT

Finding and exploring non-noble metal-based electrocatalysts for the promising power-to-hydrogen fuel technology through water splitting reactions is highly emerging. Herein, we report the preparation of cobalt-based metal-organic frameworks (Co-MOFs) using an oleylamine (OLA) and 1-dodecanethiol (DDT)-modified trimesic acid (TMA), and cobalt precursor. Then, the electrocatalytically active cobalt selenides were derived from the Co-MOFs by a water-organic solvent mixture-assisted single-step selenization process. Interestingly, the cobalt selenide obtained from the DDT-modified Co-MOF shows collectively exhaustive hydrogen evolution reaction (HER) performance with very small overpotentials of ~161 and ~206 mV to achieve 10 and 50 mA cm^{-2}, respectively, due to the phase mixing characteristics of cobalt selenide and the synergistic interaction. The fast reaction kinetics were identified at the DDT-Co selenide electrode surface as confirmed by observing the lower charge-transport/interfacial resistance and Tafel slope value due to the high surface coverage of adsorbed hydrogen (H_{ads}) atoms, evidenced by high interfacial chemical capacitance value, as a result of the high electrical conductivity and large electrochemically accessible active sites. The calculated activation energy (E_a) of HER further reveals a low kinetic energy barrier in the HER on the DDT-Co selenide, indicating high intrinsic catalytic activity due to the fast surface diffusion rate of H_{ads}. Furthermore, the obtained cathodic transfer coefficient (α_c) value strongly suggested that the HER on the surface of DDT-Co selenide ($\alpha_c = 2$) proceeds in the Langmuir-Hinshelwood reaction mechanism and follows the Volmer-Tafel pathway. The present work provides valuable insights into the modification of Co-MOFs and their impact on HER catalytic activity of cobalt selenide, and also the mechanistic investigation of HER based on electrochemical impedance spectroscopy analysis.

1. Introduction

Owing to the rapid increase in global energy scarcity and environmental pollution caused by traditional fossil fuels, tremendous efforts have been made to find promising energy sources. Hydrogen is efficient and clean energy among various energy carriers due to its zero-carbon emissions and renewable characteristics, and thus it can be a potential solution to replace gasoline-based fuels [1]. However, the major global demand for hydrogen fuel is produced by the hydrocarbon steam-reforming process in which toxic gases such as carbon monoxide and carbon dioxide are released into the environment while the production of hydrogen, making the process not environmentally friendly [2]. But, the electrocatalysts-assisted production of hydrogen gas from water molecules using electricity has been attractive since the electrocatalysts significantly lower the overpotential and increase the efficiency. Hence, hydrogen fuel production from water through an electrochemical route is expected to be a highly promising power-to-hydrogen technology due to its energy efficiency and environmental friendliness. It is well known that platinum-based electrocatalysts show outstanding electrochemical performance toward

* Corresponding author.
E-mail address: mzhou@nmsu.edu (M. Zhou).

https://doi.org/10.1016/j.apcatb.2023.122367
Received 7 October 2022; Received in revised form 29 November 2022; Accepted 2 January 2023
Available online 3 January 2023

hydrogen evolution reaction (HER) because the hydrogen adsorption free energy on the Pt surface is near zero [3]. However, the use of Pt-based catalysts for industrial-scale applications has been impeded by scarcity and high cost [3]. Therefore, extensive research has been directed toward designing and exploring inexpensive and highly abundant electrocatalysts for electrochemical HER.

In particular, transition metal sulfides/selenides/carbides/phosphides have been exploited as superior HER catalysts in an acidic medium for HER [4]. Besides, bimetallic FeIr alloy and silicide-based nanostructures have recently been explored as efficient HER electrocatalysts [5,6]. Among them, transition metal selenides have been a growing interest in electrochemical applications owing to their unique physicochemical properties, including high chemical stability and catalytic activity toward the HER [7]. Notably, cobalt diselenide ($CoSe_2$) has recently been identified as a promising low-cost material because of its high conductivity due to the presence of selenium compared to sulfur and oxygen in the transition metal-based materials, resulting in closely spaced energy bands and thus improving the electron transfer kinetics [8]. It has been reported that the HER activity in cobalt selenide can be correlated with the bond energy of Se-H_{ads}, which is very close to the value of Pt-H_{ads} (251 KJ/mol) and smaller than that of S-H_{ads} [9]. In addition, the free energy of H_{ads} on the Se sites in the cobalt selenide is comparable to that of Pt atoms, envisioning superior electrochemical performance [9]. Therefore, efforts have been made to prepare $CoSe_2$ nanostructure or form heterostructure with MXene, anchor on conductive carbon frameworks (carbon nanotubes/graphene nanosheets) or grow directly on metal/carbon substrates, and explore them as HER catalysts in acidic/basic conditions [10–12]. For example, Zhong et al. demonstrated the solvothermal assisted fabrication of graphene-like $Co_{0.85}Se$ nanostructures and investigated the effect of sulfur incorporation on the HER activity, where S-doped $Co_{0.85}Se$ was found to have a ΔG_H value of 0.067 eV, delivered much improved HER performance with a very small overpotential of 108 mV relative to the undoped $Co_{0.85}Se$ (177 mV) [13]. Attempts have also been made to synthesize the heterostructure based on Pt single atoms and nanoporous (np) $Co_{0.85}Se$, and they reported that the fabricated Pt/np-$Co_{0.85}Se$ exhibited an excellent HER with an overpotential of 55 mV compared to the bare np-$Co_{0.85}Se$ (264 mV) [14]. Furthermore, polymorphic $CoSe_2$ immobilized on mesoporous carbon nanospheres displayed superior catalytic activity (171.7 mV) towards HER than the single phase of either orthorhombic (174.5 mV) or cubic $CoSe_2$ (189.2 mV) [15]. More recently, cobalt selenides were successfully derived from the metal-organic frameworks (MOFs) as precursors/templates, which exhibited an excellent HER catalytic activity compared to cobalt selenide obtained by direct synthesis using cobalt and selenium precursors due to their high surface area and porous nature. For instance, Meng et al. prepared hexagonal cobalt selenide from ZIF-67 and then converted them to orthorhombic cobalt selenide by annealing in an inert atmosphere [16]. They found that the orthorhombic phase shows better electrocatalytic activity than the hexagonal phase of cobalt selenide [16]. Li et al. developed a Co-based bimetallic selenide ($M_xCo_{1-x}Se_2$, where M = Cu, Zn, Ni) polyhedrons that were successfully derived from the corresponding bimetallic ZIF-67 [17]. Among them, Zn-Co-based bimetallic selenide showed a lower overpotential of 140 mV compared to Ni-Co- (180 mV) and Cu-Co-based (200 mV) selenides [17]. Therefore, the fabrication of cobalt selenide nanostructures from MOFs is highly anticipated for the outstanding HER. In addition, the catalytic activity and durability of HER can generally be enhanced by coupling cobalt selenides with electrically conductive heteroatoms-doped carbon nanostructures.

In this work, trimesic acid (TMA), an organic linker, has been modified with the organic surfactants namely oleylamine (OLA) and 1-dodecanethiol (DDT), and prepared the Co-MOFs based on OLA and DDT-modified TMA (Scheme 1). Then, a one-step selenization process has been demonstrated to prepare cobalt selenides from the modified Co-MOFs using a water-organic solvent mixture. Interestingly, the $CoSe_2$ (DDT-Co selenide) derived from DDT-modified Co-MOF exhibited high catalytic activity compared to OLA-modified Co-MOF-derived $CoSe_2$ (OLA-Co selenide) and bare-Co selenide derived from unmodified Co-MOF. Notably, DDT-Co selenide yields the smallest overpotential of ~161 mV to reach 10 mA cm^{-2}, which is ~28 and ~47 mV lower than OLA-Co selenide and bare-Co selenide, respectively, revealing outstanding electrochemical performance due to the polymorphic nature of $CoSe_2$. Furthermore, electrocatalysts based on DDT-Co selenide had a much lower Tafel slope value than other catalysts, implying faster reaction kinetics at the active centers of the electrode/electrolyte interface. Moreover, it was found that the HER catalytic activity of DDT-Co selenide was considerably increased with increasing temperature, revealing high intrinsic catalytic activity as evidenced by the calculated activation energy (E_a) based on the Arrhenius relationship. More

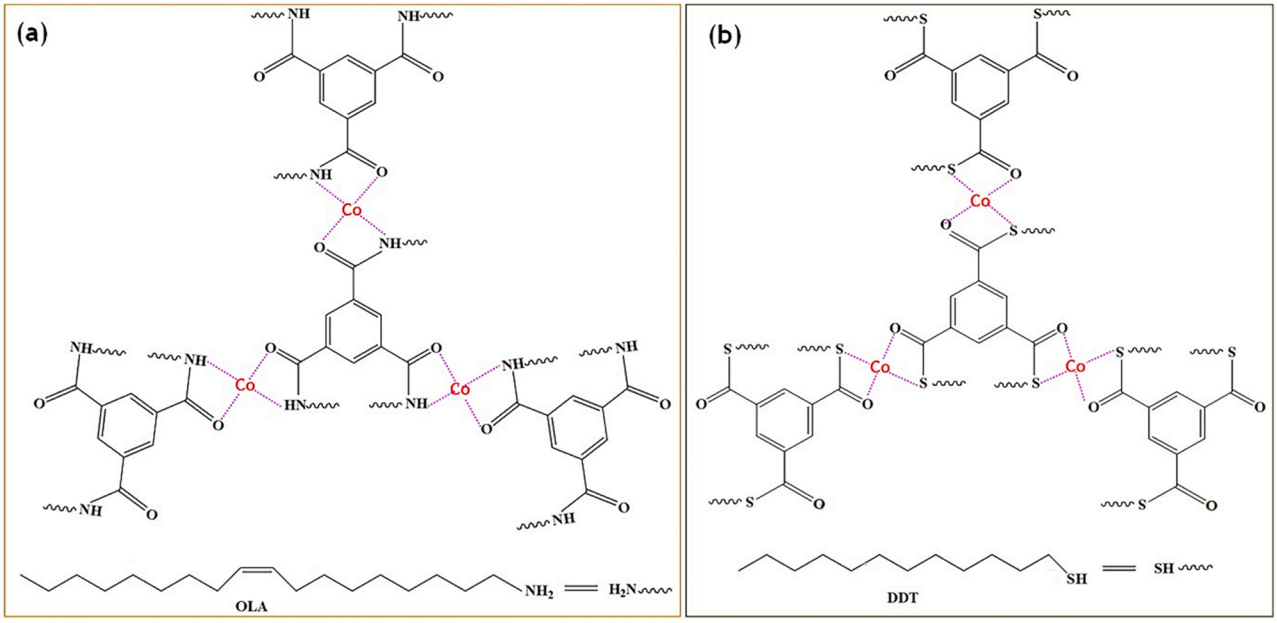

Scheme 1. The chemical structure of Co-MOF modified by (a) OLA and (b) DDT molecules.

importantly, the reaction pathway and rate-determining mechanism in the HER have been analyzed using electrochemical impedance spectroscopy (EIS) analysis through cathodic transfer coefficient (α_c) values. The electrochemical kinetic parameters obtained from EIS analysis strongly suggested that HER is a surface-controlled reaction in both OLA-Co selenide and DDT-Co selenide, where the HER proceeds in the Langmuir-Hinshelwood reaction mechanism. Moreover, the measured α_c value on the OLA-Co selenide ($\alpha_c = 1$) electrocatalyst surface indicates that the HER follows the rate-limiting chemical step next to pre-equilibrium electron transfer, implying a slow surface diffusion rate and a low concentration of surface coverage of H_{ads} ($\theta^{HER} < 1$), which was further supported by the observation of lower interfacial chemical capacitance and higher charge-transport resistance values compared to DDT-Co selenide. Whereas, the α_c value of DDT-Co selenide ($\alpha_c = 2$) corresponds to the Volmer-Tafel pathway in which the rate-determining step is the combination reaction due to the high surface coverage of the H_{ads}. The modification of TMA by organic surfactants such as OLA and DDT for the fabrication of Co-MOF and conversion to cobalt selenides for the electrochemical HER, and the determination of reaction mechanism based on α_c values have not yet been reported.

2. Experimental section

2.1. Modification of Co-MOF with oleylamine and 1-dodecanethiol

1.0 mmol trimesic acid (TMA) was dissolved in a 15 mL DMF (N, N-dimethylformamide) solution under the sonication for 15 min followed by the dropwise addition of 1 mL of oleylamine (OLA) during the sonication. It is noted that the milky white color has been immediately formed when the addition of OLA to the TMA solution owing to the modification of TMA by the OLA. A beaker containing a DMF solution of cobalt (II) nitrate hexahydrate (2 mmol, 15 mL DMF) was added to the above solution. The resulting violet-colored solution was filled in a Teflon-lined autoclave reactor (50 mL volume), and placed in an oven for 12 h at a temperature of 150 °C. For the modification of Co-MOF with 1-dodecanethiol (DDT), the above procedure was followed except for the addition of DDT instead of OLA. Finally, Co-MOF modified by OLA (violet color) and DDT (light brown color) products were obtained using vacuum filtration and then washed with ethanol solution. The collected powder samples were dried at 60 °C overnight. The obtained Co-MOF modified with OLA and DDT is denoted as OLA-Co-MOF and DDT-Co-MOF, respectively.

2.2. Synthesis of cobalt selenides from the modified Co-MOFs

3 mL hydrazine hydrate solution was added to a beaker containing an aqueous solution of sodium selenite (1.0 mmol, 15 mL distilled water), and sonicated for 15 min. Subsequently, a DMF solution containing OLA-Co-MOF or DDT-Co-MOF (100 mg, 10 mL DMF) was added to the above solution, and the resulting solution was again sonicated for 15 min. After that, the obtained final precursor solution was transferred to a Teflon-lined autoclave reactor (50 mL volume), and placed in an oven for 12 h at a temperature of 180 °C. After the reaction, the black color precipitate was collected by vacuum filtration. The obtained precipitates were washed with water and ethanol and then dried at 60 °C overnight. The cobalt selenide obtained by OLA-Co-MOF and DDT-Co-MOF is denoted as OLA-Co selenide and DDT-Co selenide, respectively. To understand the role of TMA modification by OLA and DDT in the conversion of cobalt selenide and their effect on the electrochemical HER, the cobalt selenide has also been prepared without TMA modification. The cobalt selenide obtained by using TMA without modification is denoted as bare-Co selenide.

2.3. Electrochemical measurements

Electrocatalyst ink was prepared for HER measurements as follows, 5 mg of electrocatalysts-based on cobalt selenides derived from OLA-Co-MOF, DDT-Co-MOF, and unmodified Co-MOF were dispersed in a 3:1 v/v mixture of water: isopropanol (450 μL) and 5 wt% Nafion solution (50 μL), followed by 30 min sonication. Then, the working electrode has been fabricated by the deposition of obtained ink solution to a carbon paper (CP) electrode (geometrical surface area of ~0.5 cm^2) with mass loading of ~0.7 mg cm^{-2}. The catalytic activity of different cobalt selenide nanostructures was compared with commercially acquired 20% Pt/C catalysts, where the slurry ink preparation and coating of 20% Pt/C catalysts on the CP electrode with a mass loading of ~0.7 mg cm^{-2} is similar to the preparation of cobalt selenide-based electrocatalysts. The HER electrocatalytic activity has been investigated by linear sweep voltammetry (LSV) in N_2-saturated 0.5 M H_2SO_4 electrolyte medium with a scan rate of 2 mV s^{-1}, where the Ag/AgCl reference and graphite counter electrode was used in a standard three-electrode configuration. The HER kinetics were evaluated for the OLA-Co selenide and DDT-Co selenide electrocatalysts by LSV techniques at different temperatures in 0.5 M H_2SO_4 electrolyte medium with a scan rate of 5 mV s^{-1}. The current vs. time responses of OLA-Co selenide and DDT-Co selenide were investigated at different applied overpotentials (η = 170–220 mV vs. RHE), and the long-term stability test was conducted at an applied overpotential of ~200 mV vs. RHE. The durability test for the OLA-Co selenide and DDT-Co selenide was also characterized by accelerated cyclic voltammetry (CV) measurements for 2000 cycles at a scan rate of 30 mV s^{-1}. The CV measurements were performed at various scan rates in a non-faradaic potential window to estimate the electrochemical double layer capacitance (C_{dl}) values. To determine the HER reaction mechanism, EIS measurements were conducted in the frequency range from 100 kHz to 10 mHz at an applied AC amplitude of 5 mV. Finally, the measured potentials with respect to Ag/AgCl were converted to the RHE scale based on the following relation (Eq. (1)),

$$E_{RHE} = E_{Ag/AgCl} + 0.059 \times pH + 0.197 \quad (1)$$

To estimate the turn-over frequency for the prepared electrocatalysts-based on cobalt selenides, the roughness factor (RF) was first calculated using Eq. (2) [18].

$$RF = \frac{C_{dlcatalyst}}{C_{dlflat}} \quad (2)$$

where C_{dl} catalyst is the electrochemical double layer capacitance of the prepared catalysts and C_{dl} flat is the specific capacitance of the flat standard electrode and its typical value of 40 μF cm^{-2} was used to calculate the RF [19].

Then the turn-over frequency (TOF) for the different electrocatalysts can be determined based on the following Eq. (3) [18].

$$TOF = \frac{J \times N_A}{2 \times F \times n \times RF} \quad (3)$$

where J is the cathodic current density (η = ~200 mV vs. RHE) for the electrocatalysts, N_A refers to the Avogadro's number (6.022×10^{23} mol^{-1}), n is the density of surface-active sites per cm^2 geometric area (cobalt selenide nanostructures approximately have 1×10^{16} surface sites per cm^2 [20]) and F is the Faraday constant.

The exchange current density (i_{ex}) values of OLA-Co selenide, DDT-Co selenide, and bare-Co selenide were determined according to the reported literature [21].

3. Results and discussion

3.1. Characterization of modified Co-MOFs and the derived cobalt selenides

The modification of Co-MOF with OLA and DDT was primarily confirmed by FT-IR analysis. FT-IR spectra of OLA and DDT-modified Co-MOF as shown in Fig. 1a. The attachment of DDT to the Co-MOF in

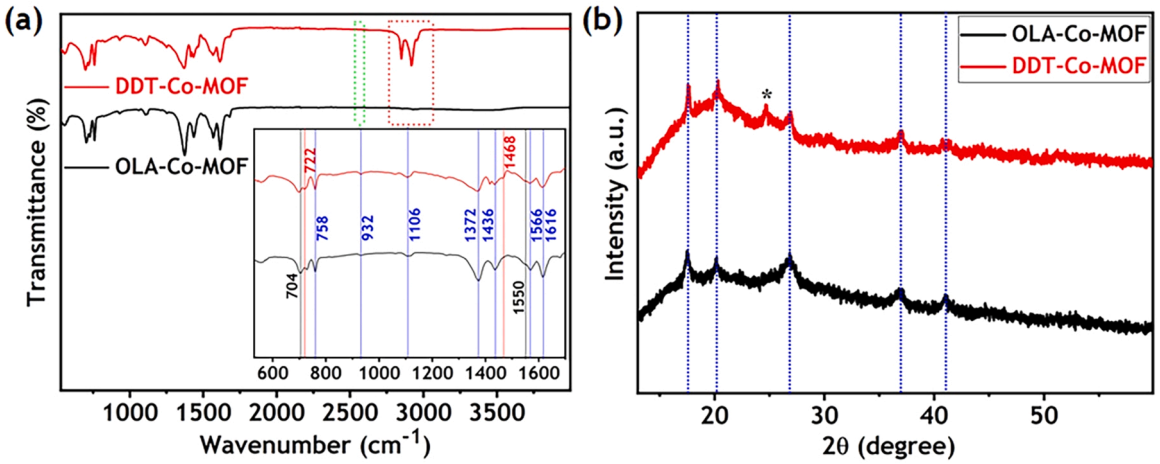

Fig. 1. (a) FT-IR and (b) XRD spectra of OLA-Co-MOF and DDT-Co-MOF.

the DDT-Co-MOF has been confirmed by observing the bands at 722, 1468 cm^{-1} and 2850, 2920 cm^{-1}, indicating the C-H bending and stretching modes of DDT, respectively [22]. It is worthy to mention here that the vibrational band around 2575 cm^{-1} was not detected in the DDT-Co-MOF, revealing the absence of S-H bond owing to the attachment of DDT to Co-MOF through sulfide linkage [23]. While the peaks detected at 704 and 1550 cm^{-1} were assigned to the vibration of C-C and amide bands, suggesting the incorporation of OLA to the Co-MOF in the OLA-Co-MOF [24,25]. The notable vibrational bands at 1566 and 1616 cm^{-1} confirm the presence of interaction between Co metal atoms and carboxylate groups [26]. The symmetric and asymmetric stretching vibration of carboxylate moieties were detected at 1372 and 1436 cm^{-1}, respectively [27]. The peaks observed at 758 and 1106 cm^{-1} result from the vibration of the benzene ring and C═O tensile vibration from the substituted TMA, respectively [28,29]. The presence of the carbonyl group attached to the O-H group can be clearly confirmed by the observation of a peak corresponding to the deformation of O-H bond at 932 cm^{-1} [30]. The above FT-IR analysis clearly indicated that OLA and DDT have been successfully attached to the Co-MOF through the amide and sulfide linkages, respectively. However, the appearance of carboxylate bands and the bands associated with the interaction between Co ions and carboxylate groups clearly suggested that the TMA has not been fully modified with either OLA or DDT, which was further confirmed by the appearance of a peak corresponding to the free TMA at 932 cm^{-1}

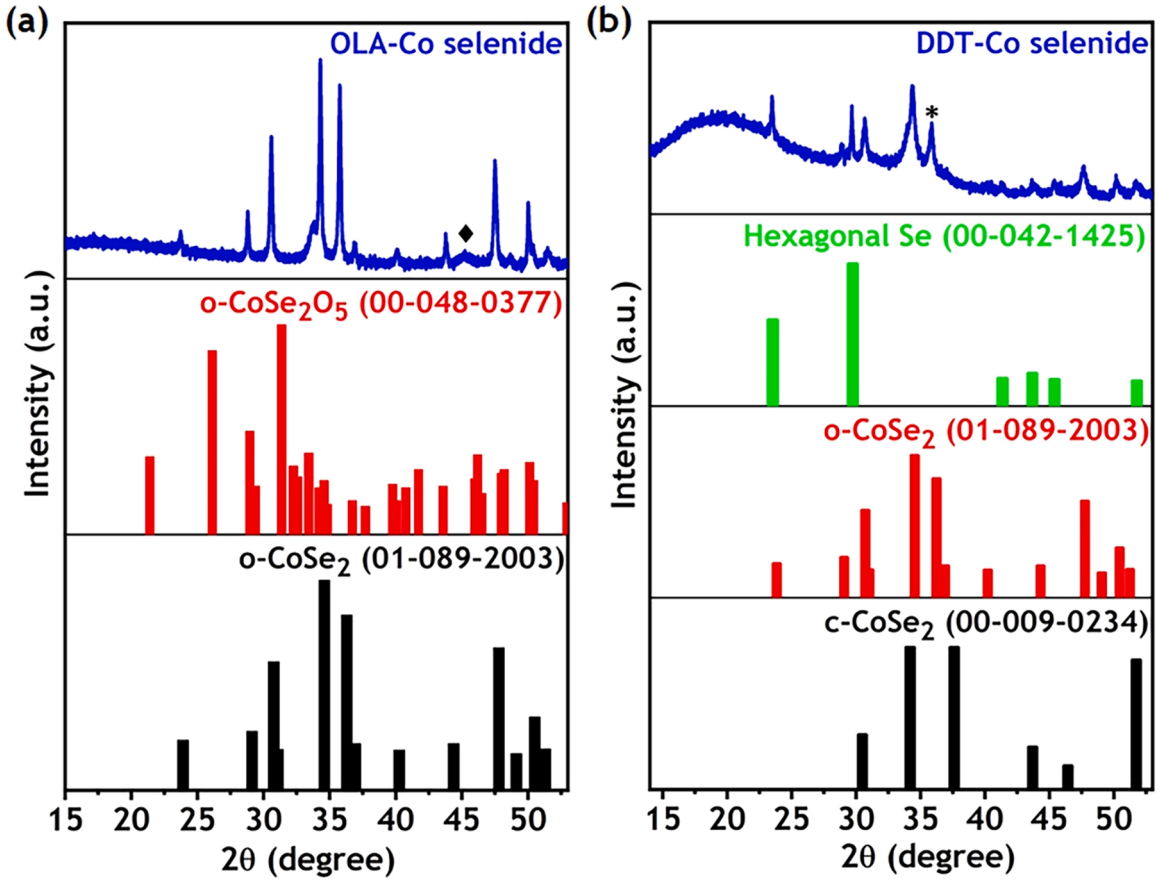

Fig. 2. XRD patterns of (a) OLA-Co selenide and (b) DDT-Co selenide with the standard reference patterns.

[30].

XRD spectra of OLA-Co-MOF and DDT-Co-MOF are depicted in Fig. 1b. It can be clearly seen that both OLA and DDT-modified Co-MOF shows similar XRD peaks at 2θ = 17.6°, 20.3°, 26.9°, 37.0°, and 41.2°, which confirmed the formation of Co-MOF since the observed diffraction lines matched well with the previously reported literature [31–33]. The absence of sharp diffraction peaks and the appearance of broad peaks with large reflections at low angles indicate the dehydration of OLA-Co-MOF and DDT-Co-MOF, and the deformation in the crystalline lattice [32,33]. It is important to mention here that an additional broad peak is found at 2θ = 24.7° in the DDT-Co-MOF compared to the OLA-Co-MOF. It may be due to the diffraction line from the methylene chain of DDT molecules [34]. In particular, no other impurity peaks were identified in both OLA-Co-MOF and DDT-Co-MOF, revealing the purity of the modified Co-MOF with OLA and DDT. The formation of cobalt selenide derived from OLA-Co-MOF and DDT-Co-MOF was characterized by XRD analysis (Fig. 2). The XRD spectra of OLA-Co selenide with the standard reference patterns of orthorhombic $CoSe_2$ (o-$CoSe_2$) (ICDD No: 01–089–2003) and orthorhombic cobalt selenite (o-$CoSe_2O_5$) (ICDD No: 00–048–0377) as shown in Fig. 2a. It has been identified that the diffraction peaks of OLA-Co selenide can be indexed to both orthorhombic phase of $CoSe_2$ and the orthorhombic phase of cobalt selenite as evidently seen in Fig. 2a. Particularly, the XRD peak position corresponding to the (111) and (120) planes of o-$CoSe_2$ was slightly shifted to a lower diffraction angle. It may be due to the incorporation of Na^+ ions into the cobalt selenide/selenite [35]. Furthermore, a detected small broad peak (identified as ◆ symbol) centered at 2θ = 45.3° indicates the presence of a small concentration of the cubic phase of metallic Se (ICDD No: 03–065–1096). Fig. 2b shows the standard reference patterns of orthorhombic (ICDD No: 01–089–2003) and cubic (ICDD No: 00–009–0234) cobalt selenide ($CoSe_2$), and hexagonal selenium (ICDD No: 00–042–1425) with the cobalt selenide derived from DDT-Co-MOF. It can be clearly seen that the major diffraction lines in the DDT-Co selenide are readily indexed to the standard reference patterns of orthorhombic and cubic phases of $CoSe_2$, implying the polymorphic nature of $CoSe_2$. Notably, the diffraction peaks observed at 2θ = 43.7° and 51.8° are mainly due to the cubic phase of $CoSe_2$ (c-$CoSe_2$), which corresponds to the (220) and (311) crystal planes,

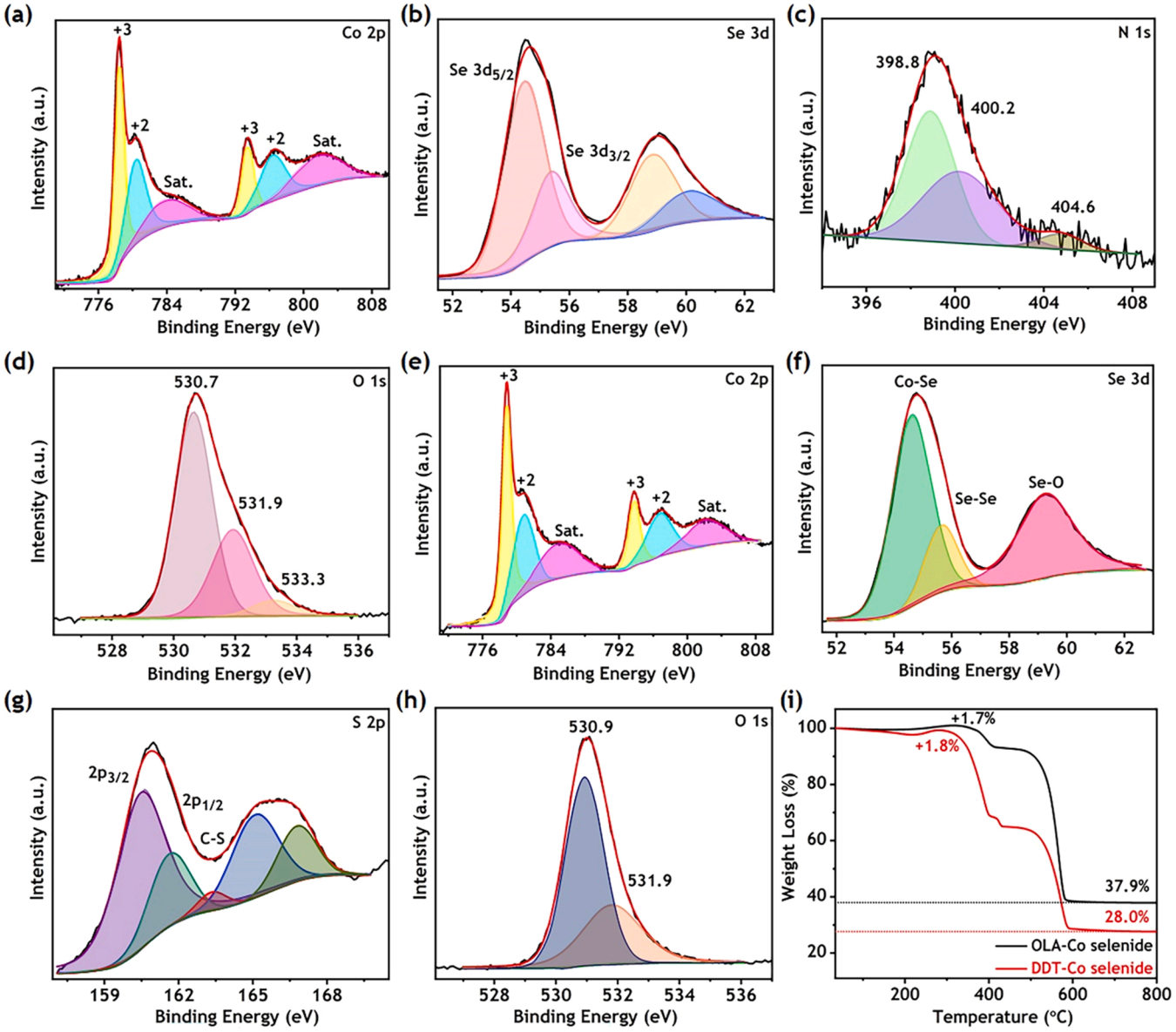

Fig. 3. (a-d) High-resolution XPS spectra of OLA-Co selenide: (a) Co 2p, (b) Se 3d, (c) N 1s, and (d) O 1s spectra. (e-h) High-resolution XPS spectra of DDT-Co selenide: (e) Co 2p, (f) Se 3d, (g) S 2p, and (h) O 1s spectra. (i) TGA analysis of OLA-Co selenide and DDT-Co selenide under air atmosphere.

respectively. Therefore, we strongly conclude that DDT-Co selenide has both cubic and orthorhombic phases of $CoSe_2$ i.e., exhibits polymorphic characteristics. However, the XRD peaks were found at $2\theta = 23.5°$, 29.7°, 41.4°, and 45.4° corresponding to the (100), (101), (110), and (111) crystal planes of Se with the hexagonal phase, respectively. The existence of metallic red Se in addition to the mixed crystalline phase of $CoSe_2$ is mainly due to the presence of DDT in DDT-Co-MOF. Since it is well known that metallic red Se has been eventually formed when thiol is combined with selenite [36]. Thus, it is highly anticipated that the more metallic cobalt selenides and the metallic red Se can be effectively derived from the DDT-Co-MOF than OLA-Co-MOF. A peak at $2\theta = 36.0°$ (identified as * symbol) is attributed to the existence of cobalt sulfide (cubic phase of Co_9S_8, ICDD No: 01–086–2273) due to the chemical reaction that takes place between thiol from DDT and Co from Co-MOF, which is in good correspondence with the XPS results.

XPS spectra of OLA-Co selenide and DDT-Co selenide are displayed in Fig. 3. The high-resolution Co 2p XPS spectra of both OLA-Co selenide and DDT-Co selenide can be resolved into six peaks, including two satellite (Sat.) peaks and two spin-orbit doublet peaks. The spin-orbit doublet peaks of Co^{3+} $2p_{3/2}$/Co^{2+} $2p_{3/2}$ and Co^{3+} $2p_{1/2}$/Co^{2+} $2p_{1/2}$ were detected at 778.4/780.4 and 793.4/796.4 eV, respectively, in the OLA-Co selenide (Fig. 3a), manifesting the presence of both $CoSe_2$ and $CoSeO_x$ moieties [9,37,38]. Whereas, the peaks at the binding energies of 778.8/780.9 and 793.8/796.8 eV in the DDT-Co selenide (Fig. 3e) are ascribed to the spin-orbit doublet peaks of Co^{3+}/Co^{2+} $2p_{3/2}$ and Co^{3+}/Co^{2+} $2p_{1/2}$, respectively [39]. It is important to mention here that the obtained XPS results are well consistent with the XRD observations. The two broad peaks in the Se 3d XPS spectra of OLA-Co selenide (Fig. 3b) splits into four separate peaks, where the peaks at 54.5 and 55.5 eV can be indexed to the binding energies of Se $3d_{5/2}$ and Se $3d_{3/2}$, respectively [40]. Whereas, a broad peak consists of two individual peaks at the binding energy ranging from 58 to 61 eV is attributed to the Se-O bonds from selenite [8,41]. The deconvoluted Se 3d XPS spectra of DDT-Co selenide (Fig. 3f) show three peaks at 54.7, 55.7, and 59.3 eV, which can be assigned to the Co-Se, Se-Se, and Se-O bonds, respectively [39]. The appearance of Se-Se peak reveals the presence of metallic Se in the DDT-Co selenide, which correlates well with the XRD results. The N 1 s spectra of OLA-Co selenide (Fig. 3c) contain three fitting peaks at 398.8, 400.2, and 404.6 eV, which are typically assigned to pyridinic-N, quaternary N, and oxidized N-atoms [42,43]. It should be noted that OLA is responsible for the doping of N-atoms in the carbon framework in addition to N-doping by hydrazine reducing agent that is attached to the cobalt selenide with selenite, which delivered outstanding electrochemical performance towards HER. As expected, N doping also takes place in the DDT-Co selenide due to the hydrazine reducing agent that was confirmed from N 1 s spectra (Fig. S1). The existence of Co-S bonding in the DDT-Co selenide owing to the formation of cobalt sulfide (Co_9S_8) due to the chemical reaction between DDT and Co atoms under high-temperature reaction conditions (180 °C for 12 h) was confirmed by observing the spin-orbit doublet peaks at 160.5 and 161.6 eV in the S 2p XPS spectra (Fig. 3g), which can be assigned to the binding energy of S $2p_{3/2}$ and S $2p_{1/2}$, respectively [44]. The peak appeared at ~163.3 eV indicating the existence of C-S bonds [45]. Also, a broad peak can be identified due to the presence of sulfate/sulfite moieties at the binding energy range between 165 eV and 170 eV [46]. The deconvoluted O 1 s spectra consisted of three and two fitting peaks in the OLA-Co selenide (Fig. 3d) and DDT-Co selenide (Fig. 3h), respectively. The peaks detected at 531.9 and 533.3 eV belong to the oxygen in the selenite and adsorbed water molecules, respectively [47,48]. Notably, the most intense peak at 530.7 or 530.9 eV originates from the oxygen in the hydroxyl group, signifying that cobalt selenide/cobalt selenite is significantly hydroxylated [47], which is responsible for boosting the electrochemical HER activity of OLA-Co selenide and DDT-Co selenide. This can be attributed to the enhancement of electrochemically accessible active site density and the improvement of the adsorption capacity of hydrogen atoms on the electrocatalyst surface.

Thermogravimetric analysis (TGA) curves of the OLA-Co selenide and DDT-Co selenide are shown in Fig. 3i, where the temperature has been increased up to 800 °C at a ramp rate of 10 °C min^{-1} under air atmosphere. The slight weight loss observed in both OLA-Co selenide and DDT-Co selenide at temperatures below 200 °C can be ascribed to the removal of adsorbed water molecules from their surface. It was found that around 1.7% and 1.8% of weight gain in the OLA-Co selenide and DDT-Co selenide at a temperature range of 230 – 340 °C and 230 – 300 °C, respectively. It can be attributed to the oxidation of metallic Se to selenium oxide and the transformation of cobalt selenide to cobalt selenate in the DDT-Co selenide [49]. Whereas the weight gain in the OLA-Co selenide can be ascribed to the oxidation of cobalt selenide/-selenite to cobalt selenate. Notably, the obvious weight loss at two or three stages in the temperature range between 400 °C and 600 °C for the OLA-Co selenide and DDT-Co selenide, indicates the sublimation of selenium oxide and the oxidation of cobalt selenate to cobalt oxide along with the combustion of carbon nanostructures [50]. In addition, the oxidation of cobalt sulfides can also be expected in the DDT-Co selenide owing to the presence of Co_9S_8 as confirmed by XRD and XPS analysis. It was noted that around 37.9 and 28.0 wt% of residual cobalt oxide can be found in the OLA-Co selenide and DDT-Co selenide, respectively.

FE-SEM and HR-TEM analysis were carried out to examine the surface morphology and elemental composition of the fabricated electrocatalysts (Fig. 4). The observed SEM images show that both OLA-Co selenide (Fig. 4a-b) and DDT-Co selenide (Fig. 4c) have a particle-like morphology. Interestingly, the ultra-small nanoparticles in both cobalt selenides were clearly observed, indicating that OLA and DDT molecules were not only used to modify the Co-MOF, but also used to control the size of the cobalt selenides, which is a dual benefit of using organic surfactants in this work. The SEM-EDS analysis of DDT-Co selenide (Fig. 4d-i) clearly confirms the uniform distribution of Co, Se, S, O, and C elements which was further confirmed by SEM-EDX analysis (Fig. S2). It is worth mentioning here that the existence of carbon and sulfur elements in the SEM-elemental mapping analysis of DDT-Co selenide revealed that the carbon nanostructures were obtained from the DDT-modified TMA moieties, and the sulfur element was incorporated into the carbon lattice by the decomposition of DDT moieties, which was further supported by XPS analysis. SEM-EDX analysis of OLA-Co selenide confirms the existence of Co, Se, N, O, and C elements (Fig. S3). The particle-like morphology of DDT-Co selenide was further confirmed by TEM analysis (Fig. 4j-k). The selected area electron diffraction (SAED) pattern of DDT-Co selenide is shown in Fig. 4l. It is evident that the polymorphic $CoSe_2$ nanoparticles were embedded in the heteroatoms-incorporated carbon nanostructures as the carbon lattice fringes at the edge of the structure were clearly identified in the HR-TEM images (Fig. 4m-n). Moreover, the observed two distinct lattice fringes in $CoSe_2$ nanoparticles (Fig. 4n) confirmed its polymorphic characteristics, which is in good agreement with XRD results.

3.2. Electrochemical HER

The electrochemical HER was evaluated for the different electrocatalysts in 0.5 M H_2SO_4 electrolyte using a standard three-electrode configuration at room temperature with a scan rate of 2 mV s^{-1}. As expected, the bare carbon paper (CP) does not have any significant HER catalytic property in the measured potential window. Whereas, both OLA-Co selenide and DDT-Co selenide deposited on CP demonstrated outstanding electrochemical performance towards HER as clearly seen in Fig. 5a (without *iR* corrections). It was found that the overpotential required for DDT-Co selenide to yield a standard cathodic current density of 10 mA cm^{-2} is ~178 mV vs. RHE, which is ~34 mV lower than OLA-Co selenide. The high HER catalytic activity observed in DDT-Co selenide is mainly attributed to its polymorphic nature as the homogeneous distribution of both cubic and orthorhombic phases of $CoSe_2$, in which the covalent nature between Co and Se atoms has been improved due to the phase mixing strategy [51]. This leads to an increase in the

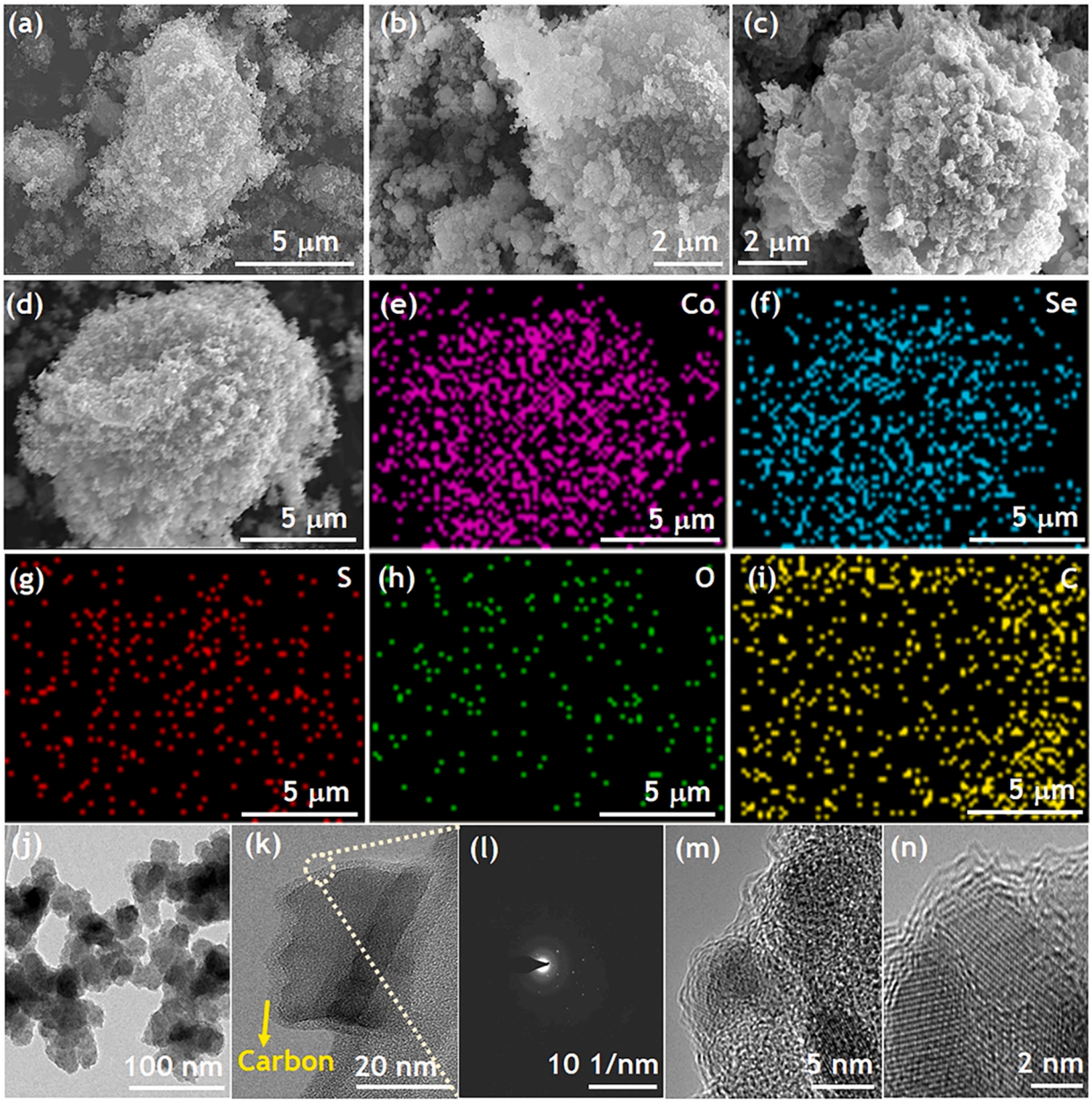

Fig. 4. FE-SEM images of (a-b) OLA-Co selenide and (c) DDT-Co selenide. SEM-EDS elemental mapping analysis of (d-i) DDT-Co selenide. TEM images (j-k) and SAED pattern (l) of DDT-Co selenide. HR-TEM images of (m-n) DDT-Co selenide.

concentration of H_{ads} on the surface of DDT-Co selenide electrocatalyst, which is further supported by EIS analysis. Moreover, the presence of metallic selenium along with polymorphic $CoSe_2$ could improve the HER activity by optimizing the hydrogen adsorption free energy and stabilizing the structure of $CoSe_2$ [52]. Additionally, the existence of Co_9S_8 in DDT-Co selenide could also promote the HER catalytic activity owing to its intrinsic HER activity. As a result, DDT-Co selenide shows the collectively exhaustive HER performance because of the phase mixing characteristics and the synergistic interaction between different species. While the OLA-Co selenide contains the combination of the orthorhombic phase of cobalt selenite and the orthorhombic phase of $CoSe_2$ leading to a slight decrease in HER catalytic activity compared to DDT-Co selenide. This may be attributed to the presence of Se-O bonds attached to the Co metal atoms in the cobalt selenite of OLA-Co selenide. Whereas, the Se atoms are directly bonded to the Co metal atoms in the DDT-Co selenide. It is important to note that the HER catalytic activity of cobalt selenides derived from both OLA-Co-MOF and DDT-Co-MOF delivered an outstanding performance compared to cobalt selenide prepared from Co-MOF using unmodified TMA. In particular, the bare-Co selenide delivers the constant current density of 10 mA cm^{-2} at a relatively high overpotential of ~230 mV vs. RHE. This clearly indicates the importance of TMA modification by OLA and DDT for the enhanced HER. In other words, it clearly reveals the impact of N and S doping in carbon nanostructures on the HER activities of OLA-Co-MOF and DDT-Co-MOF-derived cobalt selenides. Between OLA-Co selenide and DDT-Co selenide, the latter electrocatalyst showed better HER performance than the former electrocatalyst. It is due to the incorporation of S atoms into the carbon nanostructures of DDT-Co selenide in addition to the doping of N atoms by hydrazine reducing agent during the synthesis of $CoSe_2$. Whereas in the case of OLA-Co selenide, only N-doping takes place due to the modification of Co-MOF by OLA molecules, which was evidently confirmed by SEM-EDX and XPS analysis. It is important to mention here that the incorporation of N- and S-containing organic moieties into the Co-MOF can be mainly responsible for the enhancement of surface area due to the doping of N- and S/N-based moieties on the carbon nanostructures in the OLA-Co selenide and

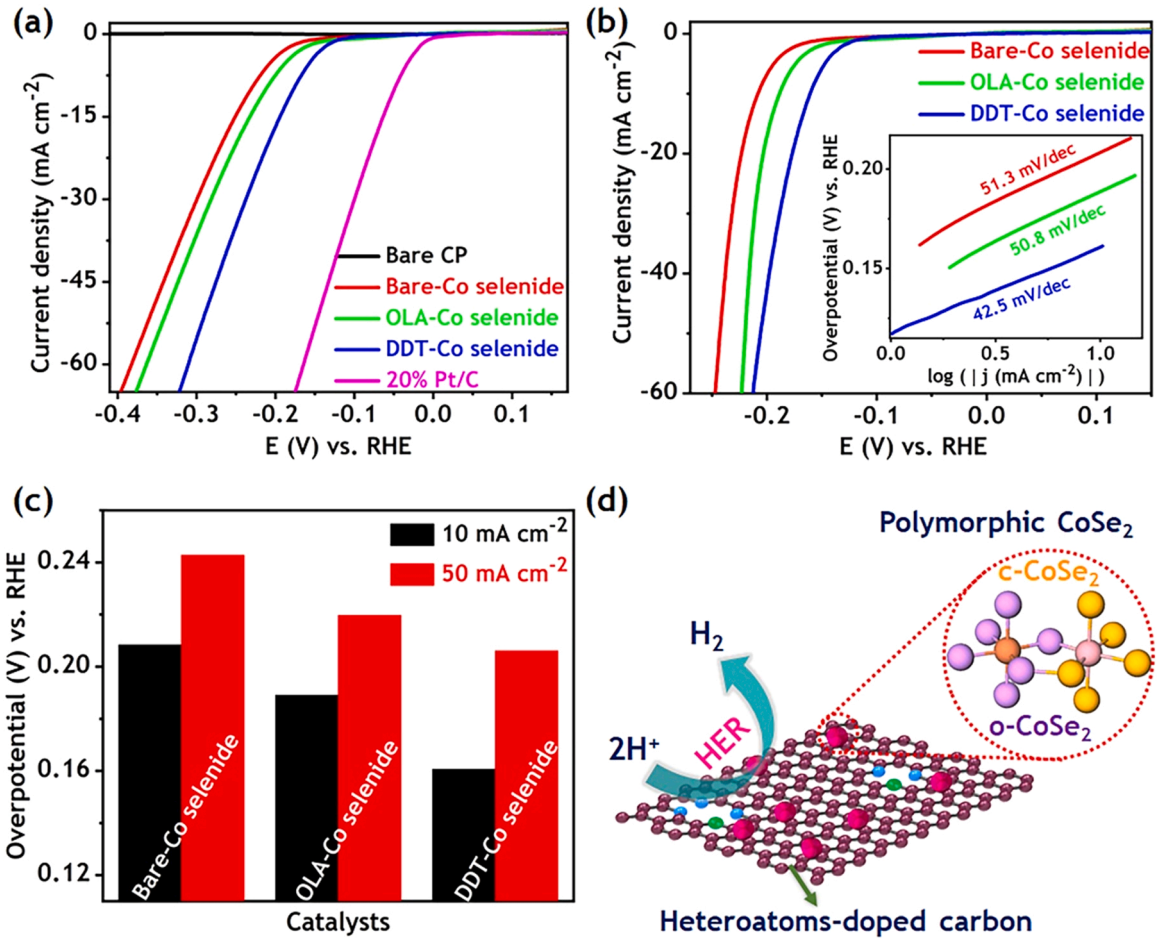

Fig. 5. Electrochemical HER performances in N_2-saturated 0.5 M H_2SO_4 solution: (a) LSV polarization curves of bare-Co selenide, OLA-Co selenide, DDT-Co selenide, and commercial 20% Pt/C. (b) *iR*-corrected LSV curves and the corresponding Tafel plots (inset) of different electrocatalysts. (c) The overpotential plots at the current densities of 10 and 50 mA cm^{-2} for the bare-Co selenide, OLA-Co selenide, and DDT-Co selenide (after *iR* corrections). (d) Schematic representation of HER process on the surface of DDT-Co selenide nanostructures.

DDT-Co selenide, respectively. Hence the fabricated DDT-Co selenide delivered higher catalytic activity with exceptional stability compared to the OLA-Co selenide. The *iR* corrected LSV polarization curves of bare-Co selenide, OLA-Co selenide, and DDT-Co selenide are displayed in Fig. 5b. It is evident that DDT-Co selenide demonstrated outstanding HER activity and required a much lower overpotential of ~161 mV than OLA-Co selenide (~189 mV) and bare-Co selenide (~208 mV), manifesting the high HER efficiency compared to other electrocatalysts. To understand the mechanistic insights and the reaction kinetics of the HER on the surface of OLA-Co selenide and DDT-Co selenide, Tafel plots were obtained from their LSV curves. As anticipated, DDT-Co selenide demonstrated a lower Tafel slope value compared to bare-Co selenide and OLA-Co selenide, confirming a faster reaction rate reflected in a very low overpotential. The Tafel slope values of bare-Co selenide, OLA-Co selenide, and DDT-Co selenide after the *iR* corrections were 51.3, 50.8, and 42.5 mV/dec, respectively (inset of Fig. 5b). Interestingly, the calculated Tafel slope value of DDT-Co selenide is much smaller than those of other electrocatalysts and some recently reported highly efficient HER electrocatalysts based on non-noble materials (Table S1). The overpotentials required to attain 10 mA cm^{-2} (η_{10}) and 50 mA cm^{-2} (η_{50}) for the different electrocatalysts are compared in Fig. 5c. Notably, the lowest η_{50} value of DDT-Co selenide (~206 mV) relative to OLA-Co selenide (~220 mV) and bare-Co selenide (~243 mV), further reveals its superior HER activity. The perceived HER electrocatalytic activity on the surface of DDT-Co selenide is comparable or even better than some recently reported efficient HER electrocatalysts based on cobalt selenides (Table S1) in an acidic medium. The polymorphic $CoSe_2$ consists of cubic and orthorhombic phases attached to the surface of heteroatoms-doped carbon nanostructures where Se atoms are bonded to cobalt atoms in orthorhombic (violet-color ball, left side) and cubic (yellow-color ball, right side) crystal structures (Fig. 5d). Recently, attempts have been demonstrated to enhance the durability and catalytic activity of $CoSe_2$ in the electrochemical HER by coupling $CoSe_2$ nanostructures with conductive carbon networks or the fabrication of polymorphic structures with a high density of active sites. By obtaining a unique polymorphic $CoSe_2$ crystal structure in which two different phases such as cubic and orthorhombic phases are uniformly mixed, the covalent bonding characteristics between cobalt and selenium atoms in the crystal structure can be significantly improved due to the strong orbital hybridization between Co 3d and Se 4p, and stabilizes the electronic structures, resulting in a robust lattice structure [51]. Moreover, DFT calculations predicted that the formation of polymorphic $CoSe_2$ is thermodynamically more feasible due to the perfect lattice matching between cubic (100) and orthorhombic $CoSe_2$ (101), resulting in lower free energy on the surface of polymorphic $CoSe_2$ compared to single crystal phase of either cubic or orthorhombic $CoSe_2$, which enhances the chemisorption of H atoms and facilitates the RDS in the HER [51,53]. Therefore, $CoSe_2$ with a polymorphic crystal system is expected to deliver superior HER catalytic activity than cubic and orthorhombic $CoSe_2$. Since, the work function of polymorphic $CoSe_2$ (~3.7 eV) was found to be lower than that of orthorhombic and cubic phase, indicating excellent catalytic activity with fast reaction kinetics of polymorphic

$CoSe_2$ [51]. Owing to the above unique characteristics, our fabricated polymorphic structures of DDT-Co selenide possess excellent HER catalytic activity.

To assess the active surface area of different electrocatalysts for the electrochemical HER, the electrochemical double layer capacitance (C_{dl}) values can be measured by obtaining CV curves at various scan rates (Fig. 6a-c). As clearly seen in the plot of anodic and cathodic current density differences at ~0.78 V vs. RHE with respect to scan rate (Fig. 6d), DDT-Co selenide has a larger C_{dl} value (~4.9 mF cm^{-2}) than OLA-Co selenide (~3.3 mF cm^{-2}) and bare-Co selenide (~2.2 mF cm^{-2}), indicating higher electrochemical surface areas and large catalytically active sites that are efficiently accessible to the electrolyte in the hydrogen reduction process. Since the materials with polymorphs characteristic are generally expected to have a much greater density of catalytically active sites/surface areas [15], which is well-supported by the obtained C_{dl} value of DDT-Co selenide. One should note that bare-Co selenide obtained from TMA-unmodified Co-MOF has a lower C_{dl} value compared to the cobalt selenides derived from TMA-modified Co-MOF with OLA and DDT, which indicates the importance of heteroatoms incorporation into the carbon nanostructures in enhancing the catalytic activity by improving the surface area.

To verify the potential practical application of OLA-Co selenide and DDT-Co selenide, durability testing was conducted using chronoamperometric and accelerated stability tests. It is apparent that the fabricated DDT-Co selenide (Fig. 7b) showed higher cathodic current density in all chronoamperometric responses at different applied overpotentials (170–220 mV) than OLA-Co selenide (Fig. 7a) due to its excellent HER catalytic activity. Moreover, it can be clearly seen that both OLA-Co selenide and DDT-Co selenide showed excellent long-term stability in the chronoamperometric testing operation at the applied overpotential of ~200 mV vs. RHE (Fig. 7c). A slight loss in catalytic activity was observed in both OLA-Co selenide and DDT-Co selenide after 22 h of continuous operation. It is worth noting that the perceived long-term stability in DDT-Co selenide relative to OLA-Co selenide is mainly attributed to the structural stability of cobalt selenide as a result of lattice robustness due to the combination of phase mixing of $CoSe_2$ and the existence of metallic Se. The stability test for the OLA-Co selenide and DDT-Co selenide was also characterized by accelerated CV measurements recorded for 2000 cycles at the scan rate of 30 mV s^{-1} (Fig. 7d). Interestingly, the polarization curve of the 2000th cycle in both OLA-Co-selenide and DDT-Co selenide has a small potential shift compared to their 1st polarization curve. It should be noted that the overpotential (η_{100}) enhancement was only ~ 20 and ~ 27 mV after 2000 cycles in the DDT-Co selenide and OLA-Co selenide, respectively, manifesting the robustness of the catalytic layer based on cobalt selenides derived from OLA-Co-MOF and DDT-Co MOF. The obtained durability tests suggest that the fabricated DDT-Co selenide contains an extremely stable polymorphic phase structure of cobalt selenide combined with S-and N-doped carbon nanostructures, leading to delivering higher catalytic activity with exceptional stability compared to the OLA-Co selenide, where the cobalt selenide/selenite combined with N-doped carbon nanostructures.

To understand the change in morphology, crystal phase and chemical environment, XRD, XPS and FE-SEM analysis were performed for the DDT-Co selenide electrocatalyst deposited on the CP electrode after the long-term durability test. Fig. S4 shows the XRD patterns of bare CP, DDT-Co selenide (fresh sample), and DDT-Co selenide deposited on CP after the long-term durability test. It can be clearly seen that all the

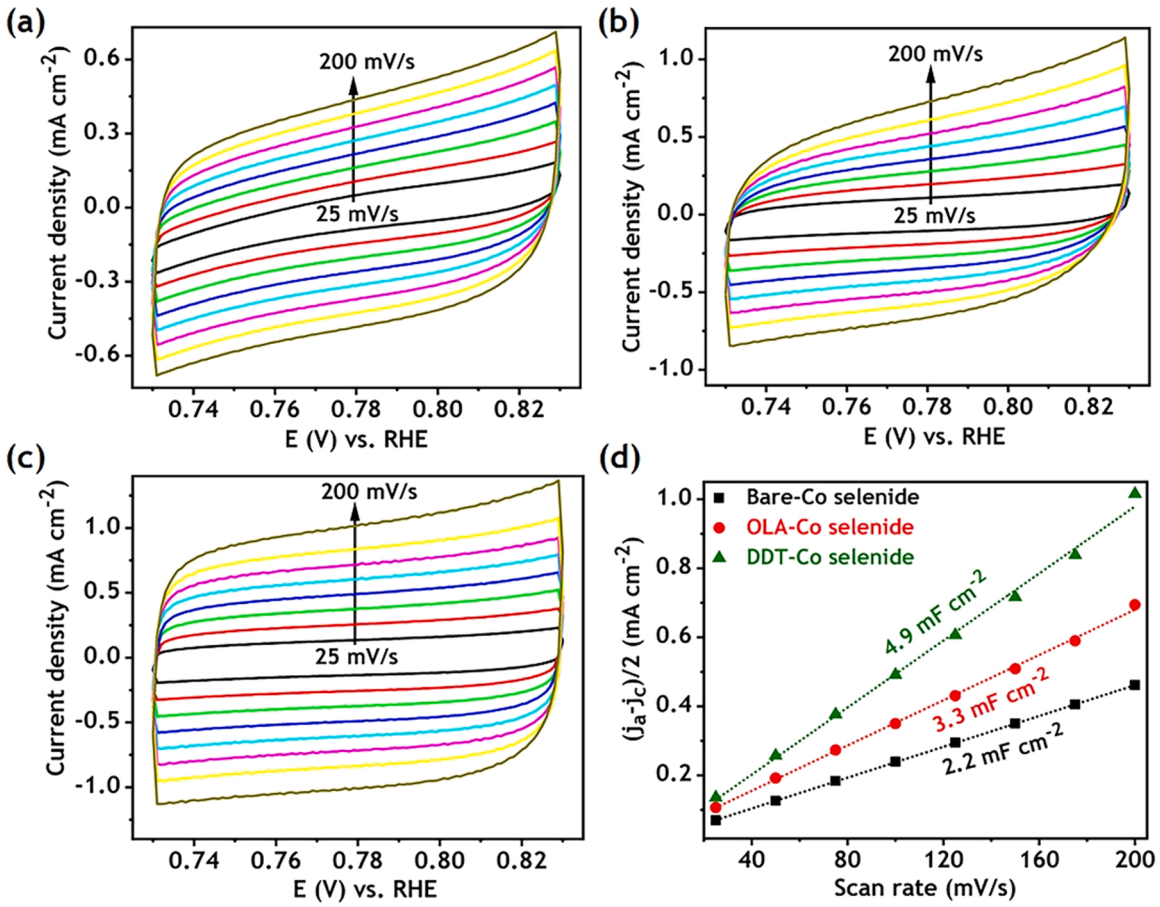

Fig. 6. CV curves of (a) bare-Co selenide, (b) OLA-Co selenide, (c) DDT-Co selenide at various scan rates in N_2-saturated 0.5 M H_2SO_4 solution, and their corresponding (d) charging current density differences as a function of scan rate at ~0.78 V vs. RHE.

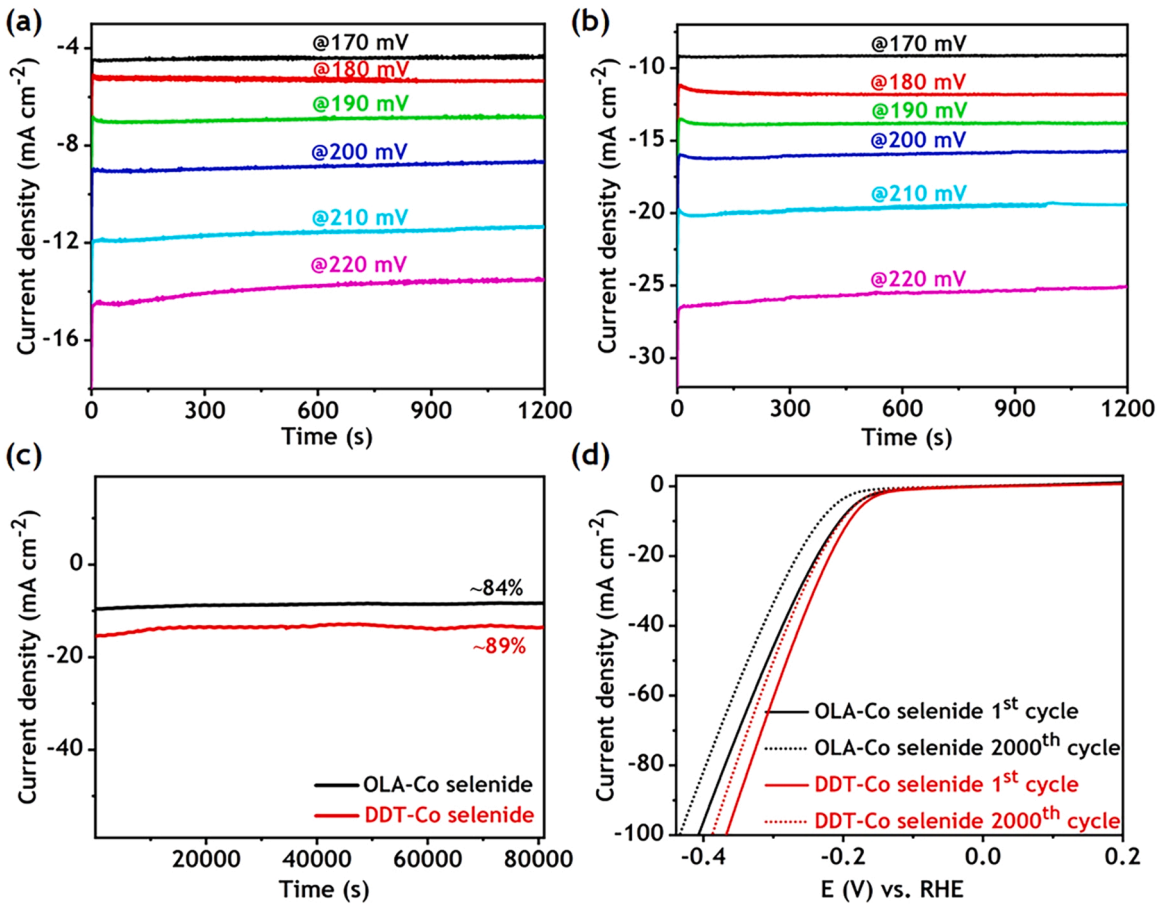

Fig. 7. Chronoamperometric responses of (a) OLA-Co selenide and (b) DDT-Co selenide at different applied overpotentials. (c) The long-term chronoamperometric stability tests of OLA-Co selenide and DDT-Co selenide at an overpotential of ~200 mV vs. RHE. (d) LSV polarization curves of before and after 2000 CV cycles of OLA-Co selenide and DDT-Co selenide (without *iR* corrections).

diffraction peaks of DDT-Co selenide coated on CP after the long-term durability test matched well with DDT-Co selenide before the durability test (fresh catalyst), indicating the strong structural stability of polymorphic $CoSe_2$. While, the characteristic hexagonal Se diffraction peaks at $2\theta = 23.5°$, 29.7°, 41.4°, and 45.4° completely disappeared after the long-term durability test, which can be attributed to the dissolution of Se and/or the formation of selenium oxide species by oxidation of metallic selenium on the surface of DDT-Co selenide during the electrochemical HER. Fig. S5 shows the XPS spectra of DDT-Co selenide deposited on CP after the long-term durability test. Alike to the Co 2p XPS spectra of DDT-Co selenide fresh catalyst, spin-orbit doublet peaks of Co^{3+} and Co^{2+} oxidation states were detected in the deconvoluted Co 2p spectra of DDT-Co selenide after the stability test (Fig. S5a), indicating the structural stability of polymorphic $CoSe_2$ during the electrochemical HER process in an acidic medium. However, the intensity of Co^{3+} signals was reduced compared to Co^{2+} peaks after the stability test. It can be attributed to the reduction of Co^{3+} to Co^{2+} during the hydrogen gas evolution process on the surface of DDT-Co selenide and/or the formation of cobalt oxide species with + 2 oxidation state due to the oxidation of cobalt selenides during the HER process [54]. Three individual peaks at the binding energies of 54.7, 55.6, and 59.5 eV were identified in the deconvoluted Se 3d spectra (Fig. S5b). The peaks at 54.7 and 55.6 eV correspond to the binding energies of Se $3d_{5/2}$ and Se $3d_{3/2}$, respectively, confirming the existence of cobalt selenides in the DDT-Co selenide after the long-term durability test [55]. Besides, the peak at 59.5 eV is attributed to the Se-O bonds [39]. It should be noted here that the intensity of Se-O bonds is noticeably increased compared to the fresh sample due to the formation of selenium oxides on the surface of DDT-Co selenide as a result of the oxidation of metallic selenium during the electrochemical HER, which is in good agreement with XRD analysis. The spin-orbit doublet peaks of S 2p were clearly observed in the deconvoluted S 2p XPS spectra of DDT-Co selenide (Fig. S5c), revealing the stability of cobalt sulfide even after the long-term stability testing. In addition, a broad peak between 163 eV and 167 eV is attributed to the surface sulfate/sulfite species [46]. Whereas new additional peaks at the higher binding energies of 168.5 and 169.8 eV were assigned to S═O and O═S═O bonds, respectively, due to the presence of Nafion binder molecule on the surface of DDT-Co selenide [56]. The deconvoluted O 1 s peaks (Fig. S5d) were observed at the binding energies of 531.7, 533.3, and 535.1 eV which can be assigned to the Se-O bonds, adsorbed H_2O molecules, and oxygen in the Nafion binder molecules, respectively [57,58]. FE-SEM analysis was performed to evaluate the morphological change of DDT-Co selenide after 22 h durability test (Fig. S6). It can be clearly seen that the morphology of DDT-Co selenide deposited on the CP electrode is well maintained even after 22 h durability test, which further reveals the robust structural stability DDT-Co selenide, where the particles were well interconnected compared to the fresh catalyst.

3.3. Electrochemical HER at different temperatures

We examined the effect of temperature on the HER kinetics of OLA-Co selenide and DDT-Co selenide electrocatalysts in 0.5 M H_2SO_4 medium at a scan rate of 5 mV s^{-1}, where a sealed electrochemical cell was placed in a thermostatic water bath. The set point of thermostatic water bath temperature was adjusted to achieve the desired temperature

(25–65 °C) inside the electrochemical cell. The temperature-dependent LSV curves of OLA-Co selenide and DDT-Co selenide are shown in Fig. 8a and b, respectively. It can be clearly seen that the HER electrocatalytic activity of both OLA-Co selenide and DDT-Co selenide was significantly increased with increasing temperature as evidently seen in increasing the cathodic current density. This indicates that the reaction rate increases with increasing temperature by lowering the energy barrier in the HER. The η_{50} values for the OLA-Co selenide and DDT-Co selenide at different temperatures are compared in Fig. 8c. It shows that the overpotentials decreased linearly with increasing temperature in both electrocatalysts. To determine the HER activation energy (E_a) for the synthesized electrocatalysts, Arrhenius plots were constructed (Fig. 8d). The E_a of OLA-Co selenide and DDT-Co selenide can be calculated based on the slope value that can be obtained from the fitting of the line in the plot of logarithm of the exchange current density (i_0) against the f (1/T) using the following relation [59] (Eq. (4))

$$E_a = -2.303R\frac{\partial(\log i_0)}{\partial(1/T)} \quad (4)$$

where R and T are the universal gas constant and absolute temperature (K), respectively. From the slope of the fitted line, E_a was calculated based on the relationship (slope = $-E_a/2.303$ R) and found to be 16.2 and 22.0 KJ mol^{-1} for the DDT-Co selenide and OLA-Co selenide, respectively. The observed smaller activation energy of DDT-Co selenide is due to a reduced energy barrier compared to OLA-Co selenide, reflecting a higher intrinsic catalytic activity due to the high surface diffusion rate of H_{ads} and have a large electrochemically accessible active surface area for the HER.

The intrinsic electrochemical activity was evaluated for the synthesized electrocatalysts by calculating the TOF per active surface site ($\eta = \sim 200$ mV, after *iR* corrections) and i_{ex} values. The calculated TOF and i_{ex} values of DDT-Co selenide are much higher than those of OLA-Co selenide and bare-Co selenide (Fig. S7), which reveals the high intrinsic HER activity due to the polymorphic characteristics of cobalt selenide with a high density of electrochemically active sites, and the fast electron-transfer kinetics in the HER.

3.4. Mechanistic interpretations of HER based on Tafel plots and EIS analysis

In order to optimize an electrocatalytic reaction, understanding the processes taking place at the electrode surface is very crucial. Typically, a heterogeneous catalytic process involves the adsorption of reactants on the catalyst surface, then the catalytic reaction proceeds, and the final step is the desorption process. There are two different mechanisms such as Langmuir–Hinshelwood and the Eley–Rideal mechanism are generally observed during the adsorption of reactants that can be transformed into products on the surface of catalysts. In the Langmuir–Hinshelwood mechanism, the reactants are adsorbed on the surface and diffused to the catalytically active sites of the catalysts. Then, the catalytic reaction takes place on the active sites to form products that are still adsorbed on the surface of the catalysts. Therefore, the final step is that the products are desorbed from the catalyst surface and leaving the catalytically active sites. Whereas in the latter mechanism, one of the reactants is

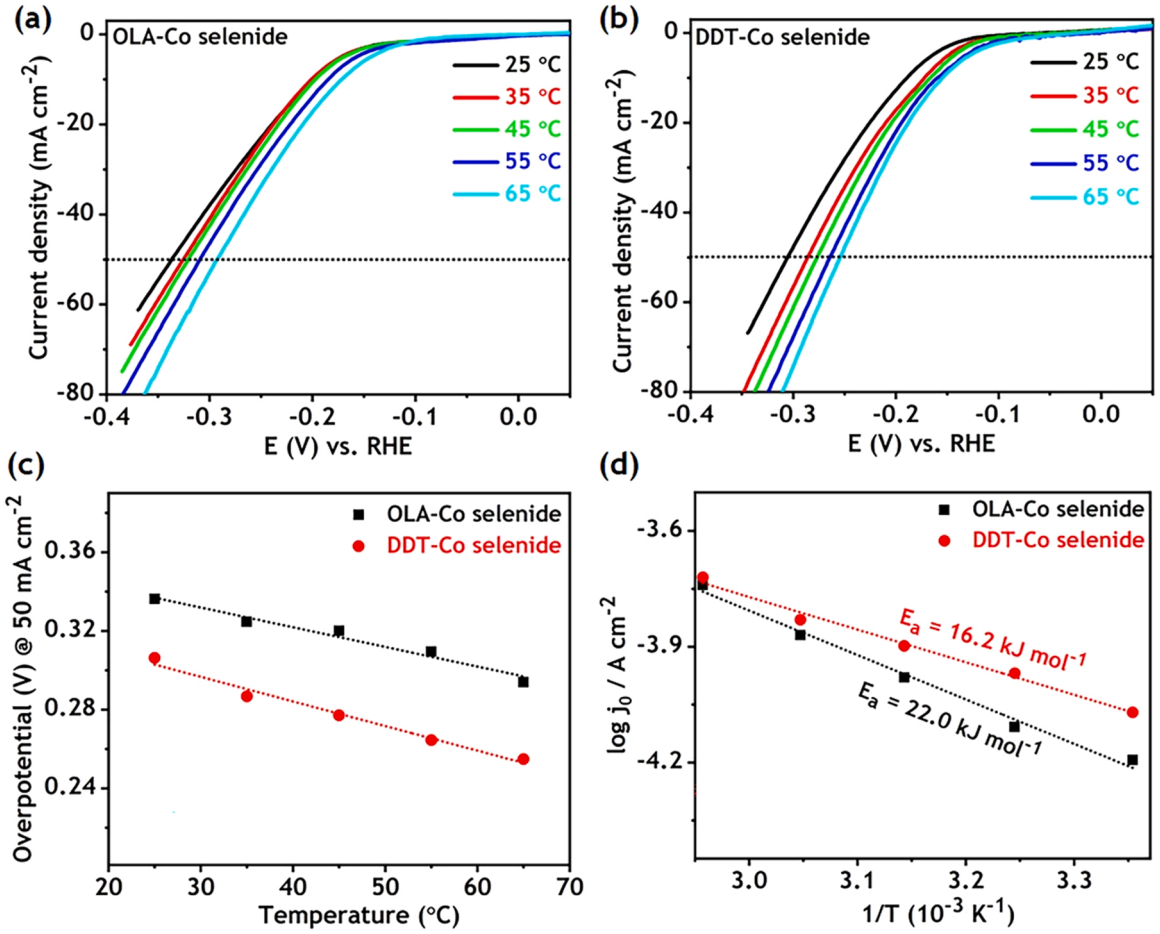

Fig. 8. LSV polarization responses of (a) OLA-Co selenide and (b) DDT-Co selenide at different temperatures (25–65 °C) (without *iR* corrections). (c) The overpotentials at a current density of 50 mA cm^{-2} as a function of operating temperatures for the OLA-Co selenide and DDT-Co selenide (without *iR* corrections). (d) Arrhenius plots as a function of temperature for the electrochemical HER on the OLA-Co selenide and DDT-Co selenide.

adsorbed on the surface of the catalyst, while the other reactants interact directly with it, resulting in the formation of products without the need for additional active or adsorption sites on the surface of the catalysts. Therefore, identifying the adsorption mechanism of the reacting species on the surface of the prepared electrocatalysts and determining the rate-determining step (RDS) in the HER is very crucial for understanding the reaction pathway and electrocatalyst performance/efficiency.

Generally, HER on the surface of typical electrocatalysts in an acidic medium follows three possible reaction steps (Eqs. (5)–(7)) [4] as shown below.

Step 1: Volmer step:

$$H_3O^+ + e^- \rightarrow H_{ads} + H_2O \quad (5)$$

Step 2: Tafel step:

$$H_{ads} + H_{ads} \rightarrow H_2 \quad (6)$$

Step 3: Heyrovsky step:

$$H_{ads} + H_3O^+ + e^- \rightarrow H_2 + H_2O \quad (7)$$

The HER pathway follows a Volmer-Heyrovsky or Volmer-Tafel step, where the reaction mechanism strongly depends on the unique surface morphology/composition and electronic properties of the fabricated electrocatalysts. Once we identify the RDS, we can optimize the binding

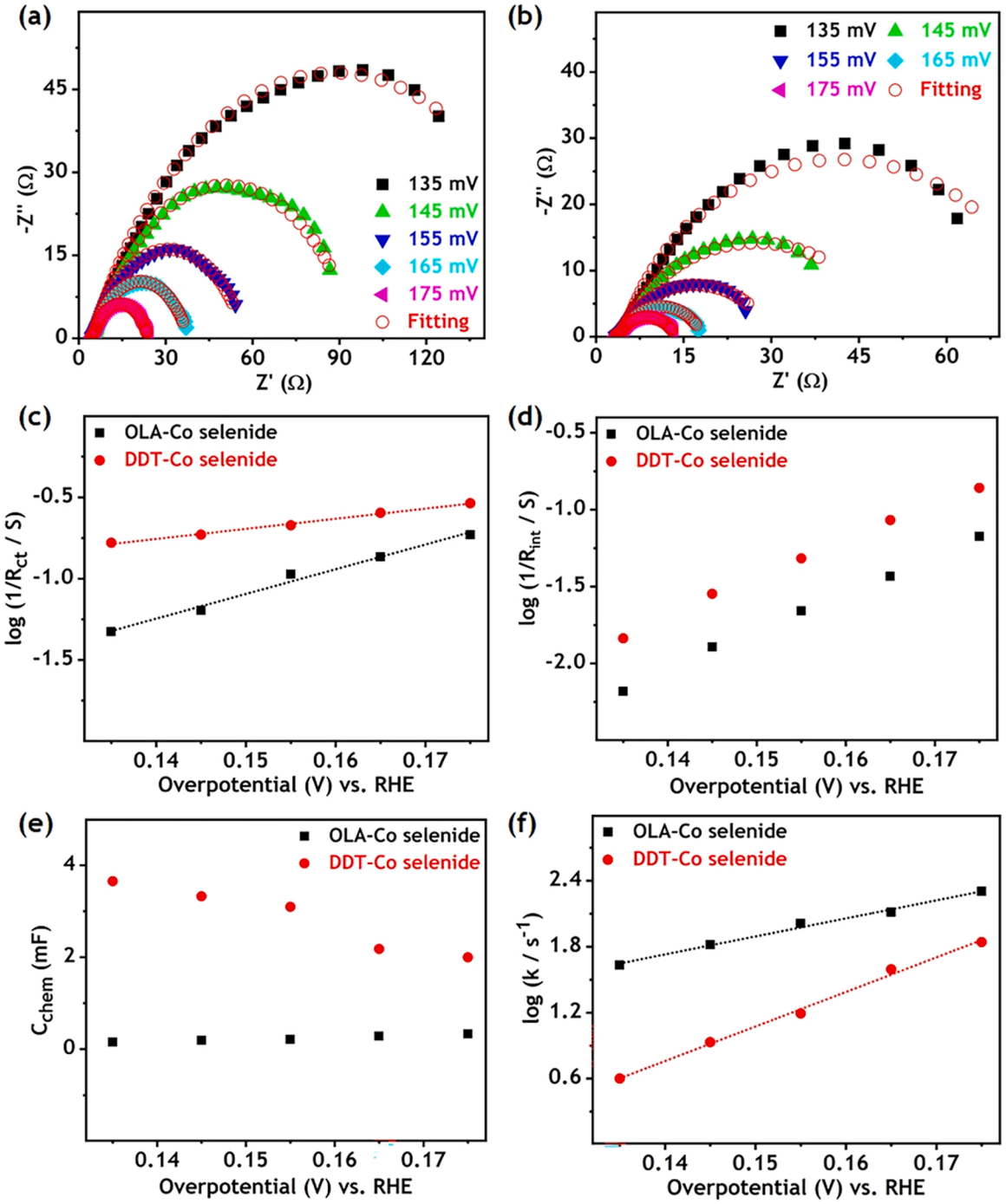

Fig. 9. EIS spectra of (a) OLA-Co selenide and (b) DDT-Co selenide at different applied overpotentials. (c) Charge-transport resistance (R_{ct}), (d) Interfacial resistance (R_{int}), (e) Interfacial chemical capacitance (C_{chem}), and (f) Reaction rate constant (k) of OLA-Co selenide and DDT-Co selenide.

strength of the electrocatalyst to the hydrogen atoms, thereby improving the HER performance. The RDS in the HER in an acidic medium can be generally determined based on the Tafel slope values that were calculated from the LSV curve, and the transfer coefficient values obtained from EIS analysis. Therefore, we have constructed the Tafel plots for the OLA-Co selenide and DDT-Co selenide from their corresponding LSV curves (inset of Fig. 5b). The Tafel slopes of 50.8 and 42.5 mV/dec can be acquired from the Tafel plots for the OLA-Co selenide and DDT-Co selenide, respectively, signifying the superiority of HER with faster reaction kinetics in the DDT-Co selenide due to the strong coupling between high metallic conductivity of mixed-phase of $CoSe_2$ and the electrically conductive N/S-doped carbon nanostructures that were derived from the organic moieties in the DDT-Co-MOF with abundant catalytically active sites for the HER. However, it is important to note here that although there is insightful information regarding HER performance based on Tafel slope value, but it is not significantly unique enough to determine and represent the true RDS [60]. Since the Tafel slope value is strongly dependent on the surface concentration of H_{ads}, where the surface coverage of H_{ads} changes significantly when changing the potential i.e., the potential dependent surface coverage of H_{ads}, but its value is usually assumed to be the constant values of 0 or 1 based on the RDS. Hence, the experimentally measured Tafel slope is often found in the intermediate value or a larger deviation from the theoretical Tafel slope values (30, 40 and 120 mV/dec) indicating a dominant change in the surface coverage of H_{ads}. Furthermore, despite the *iR* correction, the experimentally measured Tafel slope does not take into account the surface diffusion process, which is a typical phenomenon observed in heterogeneous catalysis involving hydrogen/oxygen evolution reactions. In other words, Eqs. (5)–(7) alone cannot describe overall HER pathways.

To advance our understanding of the HER performance and determine the true RDS, we carried out the EIS analysis for the OLA-Co selenide (Fig. 9a) and DDT-Co selenide (Fig. 9b) at different applied overpotentials, and the obtained EIS results were fitted with an equivalent circuit (Fig. S8). EIS analysis for the bare-Co selenide is displayed in Fig. S9. The kinetic parameters such as interfacial resistance (R_{int}), interfacial chemical capacitance (C_{chem}), and charge-transport resistance (R_{ct}) were extracted from the fitting results of OLA-Co selenide and DDT-Co selenide. The rate constant (k) which is obtained by $k = 1/(R_{int} \times C_{chem})$ allows for determining the cathodic transfer coefficient (α_c) value from the slope of log(k) vs. E (Fig. 9f). One obtains α_c values of 1 and 2 for OLA-Co selenide and DDT-Co selenide, respectively. The α_c value provides information about RDS in the HER, it can be expressed as $\alpha_c = n_r + n_q\beta_c$ where n_r and n_q represent the number of electrons transported before RDS and involved in the RDS, respectively. The value of n_q depends on 0 or 1 when the chemical or electrochemical step is the RDS. The symmetry factor (β_c) has a value that lies between 0 and 1, usually (β_c) of 0.5 is assumed. In the case where the RDS is a combination reaction, the cathodic transfer coefficient is expressed as $\alpha_c = \omega n_r + n_q\beta_c$ where ω is the stoichiometry coefficient [61]. Typical values of the cathodic transfer coefficient are reported in Table S2.

Based on the experimental values of the α_c, one can exclude an Eley-Rideal mechanism which corresponds to the Volmer-Heyrovsky pathway for HER. But the HER on the surface of OLA-Co selenide and DDT-Co selenide follows the Langmuir-Hinshelwood mechanism which was confirmed by the calculated electrochemical kinetic parameters. In addition, the electrochemical HER in both OLA-Co selenide and DDT-Co selenide is a surface-controlled reaction. EIS results show that the charge-transport resistance (R_{ct}) of OLA-Co selenide is higher than that of DDT-Co selenide (Fig. 9c). On the other hand, the interfacial chemical capacitance (C_{chem}) for DDT-Co selenide is higher than that of OLA-Co selenide (Fig. 9e). These interfacial properties determine the RDS for these HER surface-controlled reactions. Then, the α_c value of 2 for DDT-Co selenide corresponds to the Volmer-Tafel pathway in which RDS is the combination reaction (Tafel reaction). For OLA-Co selenide, the α_c of 1 indicates the rate-limiting chemical step next to pre-equilibrium electron transfer. In other words, the rate-limiting chemical step is controlled by the concomitant slow surface diffusion as evidenced by the observation of high charge-transport resistance (R_{ct}), and low surface concentration of H_{ads} as evidenced by the reflection of low interfacial chemical capacitance (C_{chem}). Since the interfacial chemical capacitance value is directly related to the surface coverage of H_{ads}. Therefore, we strongly conclude that the HER process on the DDT-Co selenide electrode surface occurs via the Volmer-Tafel pathway following the Langmuir-Hinshelwood reaction mechanism. During HER, the first step is the Volmer reaction in which hydrogen intermediates are formed and adsorbed on the surface of the electrocatalyst. Subsequently, hydrogen molecules are generated following the Tafel reaction regardless of the pathway followed. The surface diffusion also follows Sabatier's principle: The interaction between the adsorbed hydrogen (H_{ads}) intermediate and the surface should be neither too strong nor too weak (Scheme 2). If the interaction between the H_{ads} intermediate and the surface is too strong, it is not conducive to the subsequent hydrogen desorption step allowing the surface diffusion. The role of surface diffusion in the HER following the Volmer-Tafel pathway and the determination of the RDS based on the α_c values is illustrated in Scheme 3. One has to consider two limiting cases depending upon the surface coverage of H_{ads}. When the catalysts have a low surface diffusion rate, the chemical bond formation between the two H_{ads} to yield H_2 is controlled by the surface diffusion as the time-dependent probability of interaction between the two H_{ads} decreases. Accordingly, surface diffusion is considered as the RDS in the HER on the surface of OLA-Co selenide as strongly indicated by the calculated α_c and $1/R_{ct}$ values. On the other hand, if the catalysts have a high surface diffusion rate and high surface coverage of the H_{ads}, then the H-H bond formation is the RDS. One observes this behavior for the DDT-Co selenide surface in which the H-H bond formation is considered to be the RDS as indicated by the observed α_c and interfacial capacitance C_{chem} values. For both limiting cases, the final step is the desorption of H_2 molecules and leaves the active site for the adsorption of hydrogen atoms. The schematic representation of the HER controlled surface reactions according to Langmuir-Hinshelwood reaction mechanisms following the Volmer-Tafel pathway involves the surface diffusion process and determination of RDS in the HER based on α_c values on the surface of OLA-Co selenide and DDT-Co selenide is shown in Scheme 3a and b, respectively. The above mechanistic investigation of HER electrocatalysts based on cobalt selenide nanostructures has not yet been demonstrated in the literature.

4. Conclusions

We successfully derived the cobalt selenide nanostructures from the Co-MOFs modified with OLA and DDT. The obtained DDT-Co selenide showed an impressive electrocatalytic HER activity and durability than OLA-Co selenide due to the polymorphic features of cobalt selenide strongly coupled to heteroatoms-doped carbon nanostructures. The fast catalytic HER rate at the DDT-Co selenide electrode was confirmed by EIS and Tafel slope analysis. Moreover, we have investigated the temperature effect on the HER catalytic activity of the prepared electrocatalysts and found that the overpotentials decrease linearly with increasing temperature due to the lowering of the energy barrier in the HER. The measured E_a reveals the high intrinsic catalytic activity of DDT-Co selenide resulting from the low kinetic barrier and high surface diffusion rate of H_{ads} in the HER. We also demonstrated the HER mechanistic investigation of cobalt selenide nanostructures based on α_c values, and found that the HER at the DDT-Co selenide electrode follows the Volmer-Tafel pathway. While in the OLA-Co selenide, the rate-limiting chemical step is controlled by the concomitant slow surface diffusion, attributed to the low hydrogen coverage ($\theta^{HER} < 1$) as strongly confirmed by the interfacial chemical capacitance value. This work can be exploited to modify the MOFs based on different transition metal atoms and their conversion into catalytically active electrocatalysts for the promising electrochemical applications. In addition, the

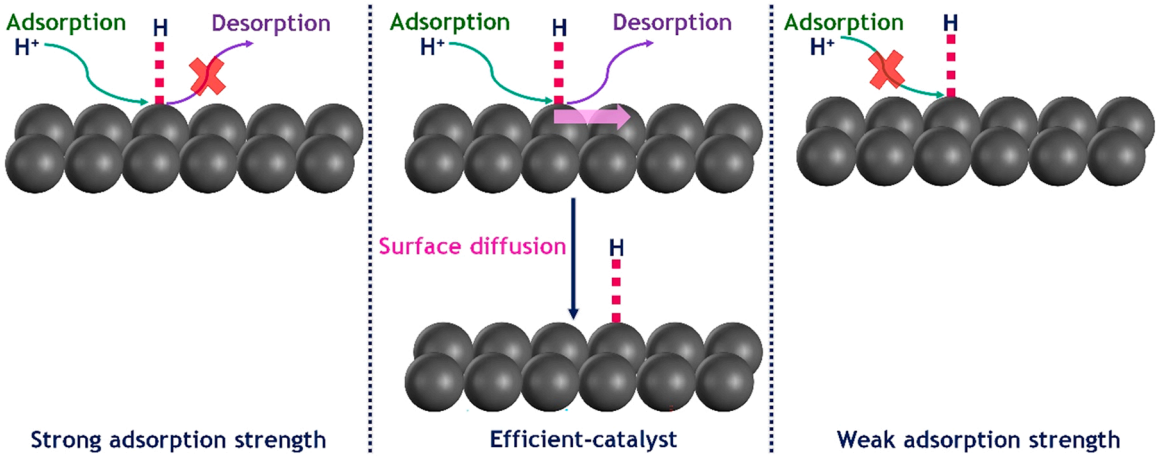

Scheme 2. Surface diffusion according to Sabatier's principle.

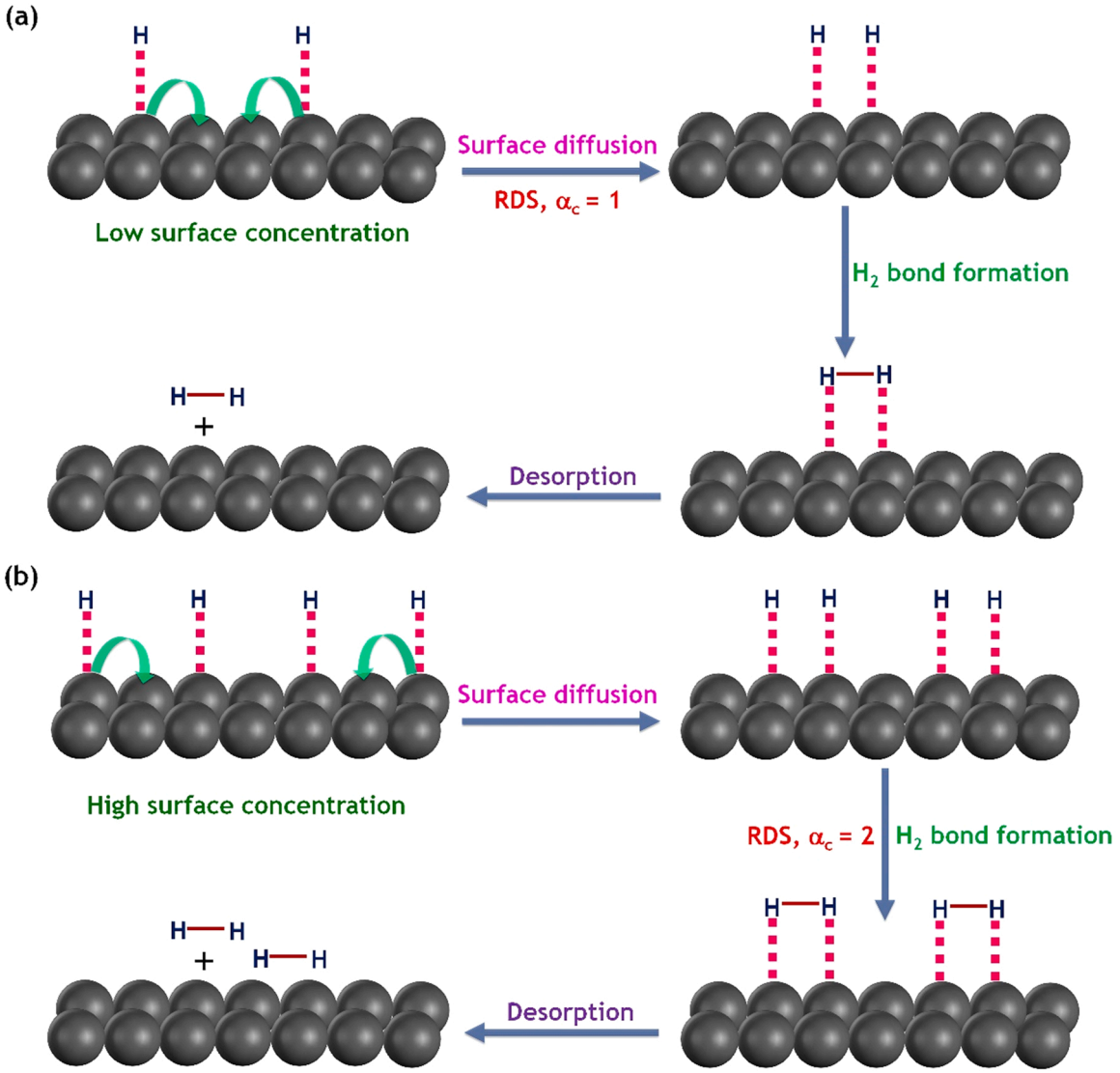

Scheme 3. HER controlled surface reactions according to Langmuir-Hinshelwood reaction mechanisms on the surface of (a) OLA-Co selenide and (b) DDT-Co selenide electrocatalysts.

demonstrated EIS analysis will help to understand the HER reaction mechanism and determine the true RDS on the surface of different electrocatalysts.

CRediT authorship contribution statement

Pitchai Thangasamy made the main contributions from material synthesis to mechanism interpretations. Rong He helped with the material synthesis and electrochemical characterizations. Hyacinthe Randriamahazaka was involved in theoretical calculations. Xinqi Chen did the XPS characterization. Yizhi Zhang and Haiyan Wang did the HR-TEM characterizations. Hongmei Luo contributed to the design of the experiments. Meng Zhou oversaw the experiments, calculations and provided advices.

Declaration of Competing Interest

The authors declare that they have no known competing financial interests or personal relationships that could have appeared to influence the work reported in this paper.

Data availability

Data will be made available on request.

Acknowledgements

This work is supported by the U. S. National Science Foundation: OIA-2119688. H.R acknowledges Université Paris Cité and CNRS for the support. H.W. acknowledge the support from the U.S. National Science Foundation (DMR-2016453) for the TEM work at Purdue University.

Appendix A. Supplementary material

Supplementary data associated with this article can be found in the online version at doi:10.1016/j.apcatb.2023.122367.

References

[1] T. Liu, P. Diao, Z. Lin, H. Wang, Sulfur and selenium doped nickel chalcogenides as efficient and stable electrocatalysts for hydrogen evolution reaction: the importance of the dopant atoms in and beneath the surface, Nano Energy 74 (2020), 104787, https://doi.org/10.1016/j.nanoen.2020.104787.

[2] U. Gupta, C.N.R. Rao, Hydrogen generation by water splitting using MoS_2 and other transition metal dichalcogenides, Nano Energy 41 (2017) 49–65, https://doi.org/10.1016/j.nanoen.2017.08.021.

[3] S. Liu, Z. Lin, R. Wan, Y. Liu, Z. Liu, S. Zhang, X. Zhang, Z. Tang, X. Lu, Y. Tian, Cobalt phosphide supported by two-dimensional molybdenum carbide (MXene) for the hydrogen evolution reaction, oxygen evolution reaction, and overall water splitting, J. Mater. Chem. A 9 (2021) 21259–21269, https://doi.org/10.1039/d1ta05648d.

[4] M. Zeng, Y. Li, Recent advances in heterogeneous electrocatalysts for the hydrogen evolution reaction, J. Mater. Chem. A 3 (2015) 14942–14962, https://doi.org/10.1039/c5ta02974k.

[5] S. Ma, J. Deng, Y. Xu, W. Tao, X. Wang, Z. Lin, Q. Zhang, L. Gu, W. Zhong, Pollen-like self-supported FeIr alloy for improved hydrogen evolution reaction in acid electrolyte, J. Energy Chem. 66 (2022) 560–565, https://doi.org/10.1016/j.jechem.2021.08.066.

[6] S. Shen, Z. Hu, H. Zhang, K. Song, Z. Wang, Z. Lin, Q. Zhang, L. Gu, W. Zhong, Highly active Si sites enabled by negative valent Ru for electrocatalytic hydrogen evolution in LaRuSi, Angew. Chem. Int. Ed. 61 (2022), e202206460, https://doi.org/10.1002/anie.202206460.

[7] X. Peng, Y. Yan, X. Jin, C. Huang, W. Jin, B. Gao, P.K. Chu, Recent advance and prospectives of electrocatalysts based on transition metal selenides for efficient water splitting, Nano Energy 78 (2020), 105234, https://doi.org/10.1016/j.nanoen.2020.105234.

[8] Z. Li, X. Hu, Z. Shi, Z. Wang, J. Lu, Hierarchical Co_3Se_4 nanoparticles encapsulated in a nitrogen-doped carbon framework intertwined with carbon nanotubes as anode of Li-ion batteries, Energy Technol. (2021), 2100462, https://doi.org/10.1002/ente.202100462.

[9] D. Gao, B. Zhao, F. Chen, H. Yu, J. Fan, J. Yu, Selenium-rich configuration and amorphization for synergistically maximizing the active-center amount of $CoSe_{1+x}$ nanodots toward efficient photocatalytic H_2 evolution, ACS Sustain. Chem. Eng. 9 (2021) 8653–8662, https://doi.org/10.1021/acssuschemeng.1c02767.

[10] L. Hao, H. He, C. Xu, M. Zhang, H. Feng, L. Yang, Q. Jiang, H. Huang, Ultrafine cobalt selenide nanowires tangled with MXene nanosheets as highly efficient electrocatalysts toward the hydrogen evolution reaction, Dalton Trans. 51 (2022) 7135–7141, https://doi.org/10.1039/d2dt00238h.

[11] V.D. Nithya, Recent advances in $CoSe_2$ electrocatalysts for hydrogen evolution reaction, Int. J. Hydrog. Energy 46 (2021) 36080–36102, https://doi.org/10.1016/j.ijhydene.2021.08.157.

[12] Y. Li, Y. Zhao, H. Zhao, Z. Wang, H. Li, P. Gao, A bifunctional catalyst of ultrathin cobalt selenide nanosheets for plastic-electroreforming-assisted green hydrogen generation, J. Mater. Chem. A 10 (2022) 20446–20452, https://doi.org/10.1039/d2ta04286j.

[13] S. Shen, Z. Lin, K. Song, Z. Wang, L. Huang, L. Yan, F. Meng, Q. Zhang, L. Gu, W. Zhong, Reversed active sites boost the intrinsic activity of graphene-like cobalt selenide for hydrogen evolution, Angew. Chem. 133 (2021) 12468–12473, https://doi.org/10.1002/ange.202102961.

[14] K. Jiang, B. Liu, M. Luo, S. Ning, M. Peng, Y. Zhao, Y.R. Lu, T.S. Chan, F.M.F. de Groot, Y. Tan, Single platinum atoms embedded in nanoporous cobalt selenide as electrocatalyst for accelerating hydrogen evolution reaction, Nat. Commun. 10 (2019) 1743, https://doi.org/10.1038/s41467-019-09765-y.

[15] S.H. Yang, G.D. Park, J.K. Kim, Y.C. Kang, New strategy to synthesize optimal cobalt diselenide@hollow mesoporous carbon nanospheres for highly efficient hydrogen evolution reaction, Chem. Eng. J. 424 (2021), 130341, https://doi.org/10.1016/j.cej.2021.130341.

[16] J. Sun, J. Li, Z. Li, X. Hu, H. Bai, X. Meng, Phase transition in cobalt selenide with a greatly improved electrocatalytic activity in hydrogen evolution reactions, ACS Sustain. Chem. Eng. 10 (2022) 4022–4030, https://doi.org/10.1021/acssuschemeng.2c00449.

[17] X. Wang, F. Li, W. Li, W. Gao, Y. Tang, R. Li, Hollow bimetallic cobalt-based selenide polyhedrons derived from metal-organic framework: an efficient bifunctional electrocatalyst for overall water splitting, J. Mater. Chem. A 5 (2017) 17982–17989, https://doi.org/10.1039/c7ta03167j.

[18] B. Lin, Z. Lin, S. Chen, M. Yu, W. Li, Q. Gao, M. Dong, Q. Shao, S. Wu, T. Ding, Z. Guo, Surface intercalated spherical $MoS_{2x}Se_{2(1-x)}$ nanocatalysts for highly efficient and durable hydrogen evolution reactions, Dalton Trans. 48 (2019) 8279–8287, https://doi.org/10.1039/c9dt01218d.

[19] J. Fu, R. Ali, C. Mu, Y. Liu, N. Mahmood, W.M. Lau, X. Jian, Large-scale preparation of 2D VSe_2 through a defect-engineering approach for efficient hydrogen evolution reaction, Chem. Eng. J. 411 (2021), 128494, https://doi.org/10.1016/j.cej.2021.128494.

[20] A.I. Carim, F.H. Saadi, M.P. Soriaga, N.S. Lewis, Electrocatalysis of the hydrogen-evolution reaction by electrodeposited amorphous cobalt selenide films, J. Mater. Chem. A 2 (2014) 13835–13839, https://doi.org/10.1039/c4ta02611j.

[21] N. Zang, Z. Wu, J. Wang, W. Jin, Rational design of Cu-Co thiospinel ternary sheet arrays for highly efficient electrocatalytic water splitting, J. Mater. Chem. A 8 (2020) 1799–1807, https://doi.org/10.1039/c9ta12104h.

[22] Z. Zhuang, W. Chen, One-step rapid synthesis of $Ni_6(C_{12}H_{25}S)_{12}$ nanoclusters for electrochemical sensing of ascorbic acid, Analyst 145 (2020) 2621–2630, https://doi.org/10.1039/c9an01947b.

[23] R. Nyquist, Thiols, sulfides and disulfides, alkanethiols, and alkanedithiols (S-H stretching). Interpreting Infrared, Raman, and Nuclear Magnetic Resonance Spectra 2, 2001, pp. 65–83.

[24] M. Amir, A. Baykal, H. Sözeri, H. Güngüneş, S.E. Shirsath, Oleylamine surface functionalized $FeCo_yFe_{2-y}O_4$ ($0.0 \leqslant y \leqslant 1.0$) nanoparticles, Arab. J. Chem. 12 (2019) 4971–4981, https://doi.org/10.1016/j.arabjc.2016.10.010.

[25] A. Barth, Infrared spectroscopy of proteins, Biochim. Biophys. Acta 2007 (1767) 1073–1101, https://doi.org/10.1016/j.bbabio.2007.06.004.

[26] Z. Ma, J. Zou, D. Khan, W. Zhu, C. Hu, X. Zeng, W. Ding, Preparation and hydrogen storage properties of MgH_2-trimesic acid-TM MOF (TM=Co, Fe) composites, J. Mater. Sci. Technol. 35 (2019) 2132–2143, https://doi.org/10.1016/j.jmst.2019.05.049.

[27] W. Zhang, C. Huang, J. Zhu, Q. Zhou, R. Yu, Y. Wang, P. An, J. Zhang, M. Qiu, L. Zhou, L. Mai, Z. Yi, Y. Yu, Dynamic restructuring of coordinatively unsaturated copper paddle wheel clusters to boost electrochemical CO_2 reduction to hydrocarbons, Angew. Chem. Int. Ed. 61 (2022), e202112116, https://doi.org/10.1002/anie.202112116.

[28] T. Alammar, I.Z. Hlova, S. Gupta, V. Balema, V.K. Pecharsky, A.V. Mudring, Luminescence properties of mechanochemically synthesized lanthanide containing MIL-78 MOFs, Dalton Trans. 47 (2018) 7594–7601, https://doi.org/10.1039/c7dt04771a.

[29] C. Zhang, Q. Wang, W. Zhang, X. Li, Z. Zhu, C. Zhang, A. Xie, S. Luo, Preparation and application of Co_3O_4-Ni-MOF/MWCNTs hybrid for supercapacitor, Ionics 27 (2021) 3543–3551, https://doi.org/10.1007/s11581-021-04137-3.

[30] B.S. Gupta, B.P. Jelle, T. Gao, Application of ATR-FTIR spectroscopy to compare the cell materials of wood decay fungi with wood mould fungi, Int. J. Spectrosc. 2015 (2015) 1–7, https://doi.org/10.1155/2015/521938.

[31] J. Ethiraj, V. Surya, P. Selvam, J.G. Vitillo, Water-driven structural transformation in cobalt trimesate metal-organic frameworks, Energies 14 (2021) 4751, https://doi.org/10.3390/en14164751.

[32] N.S. Punde, C.R. Rawool, A.S. Rajpurohit, S.P. Karna, A.K. Srivastava, Hybrid composite based on porous cobalt-benzenetricarboxylic acid metal organic framework and graphene nanosheets as high performance supercapacitor electrode, ChemistrySelect 3 (2018) 11368–11380, https://doi.org/10.1002/slct.201802721.

[33] J.L. Crane, K.E. Anderson, S.G. Conway, Hydrothermal synthesis and characterization of a metal-organic framework by thermogravimetric analysis, powder X-ray diffraction, and infrared spectroscopy: an integrative inorganic

chemistry experiment, J. Chem. Educ. 92 (2015) 373–377, https://doi.org/10.1021/ed5000839.
[34] J. Jayabharathi, G.A. Sundari, V. Thanikachalam, P. Jeeva, S. Panimozhi, A dodecanethiol-functionalized Ag nanoparticle-modified ITO anode for efficient performance of organic light-emitting devices, RSC Adv. 7 (2017) 38923–38934, https://doi.org/10.1039/c7ra07080b.
[35] X. Liu, Z. Niu, Y. Xu, Z. Zhao, C. Li, Y. Yi, H. Guan, S. Zhang, X. Pei, D. Li, Rational design heterostructured bimetallic selenides for high capacity and durability sodium/potassium-ion storage, Chem. Eng. J. 430 (2022), 133176, https://doi.org/10.1016/j.cej.2021.133176.
[36] D. Burriss, W. Zou, D. Cremer, J. Walrod, D. Atwood, Removal of selenite from water using a synthetic dithiolate: An experimental and quantum chemical investigation, Inorg. Chem. 53 (2014) 4010–4021, https://doi.org/10.1021/ic402909t.
[37] G.D. Park, Y. Chan Kang, Amorphous cobalt selenite nanoparticles decorated on a graphitic carbon hollow shell for high-rate and ultralong cycle life lithium-ion batteries, ACS Sustain. Chem. Eng. 8 (2020) 17707–17717, https://doi.org/10.1021/acssuschemeng.0c05658.
[38] K. Ao, J. Dong, C. Fan, D. Wang, Y. Cai, D. Li, F. Huang, Q. Wei, Formation of yolk-shelled nickel-cobalt selenide dodecahedral nanocages from metal-organic frameworks for efficient hydrogen and oxygen evolution, ACS Sustain. Chem. Eng. 6 (2018) 10952–10959, https://doi.org/10.1021/acssuschemeng.8b02343.
[39] B. Hu, X. Liu, A. Liu, Y. Ren, Z. Guo, J. Mu, X. Zhang, Z. Zhang, X. Liu, H. Che, Reduced graphene oxide nanosheet-wrapped hollow cobalt selenide nanocubes as electrodes for supercapacitors, ACS Appl. Nano Mater. 4 (2021) 13267–13278, https://doi.org/10.1021/acsanm.1c02792.
[40] D. Chen, Z. Xu, W. Chen, G. Chen, J. Huang, J. Huang, C. Song, C. Li, K. (Ken) Ostrikov, Just add water to split water: ultrahigh-performance bifunctional electrocatalysts fabricated using eco-friendly heterointerfacing of NiCo diselenides, J. Mater. Chem. A 8 (2020) 12035–12044, https://doi.org/10.1039/d0ta02121k.
[41] J.S. Park, G.D. Park, Y.C. Kang, Exploration of cobalt selenite–carbon composite porous nanofibers as anode for sodium-ion batteries and unveiling their conversion reaction mechanism, J. Mater. Sci. Technol. 89 (2021) 24–35, https://doi.org/10.1016/j.jmst.2021.01.076.
[42] B.J. Matsoso, K. Ranganathan, B.K. Mutuma, T. Lerotholi, G. Jones, N.J. Coville, Time-dependent evolution of the nitrogen configurations in N-doped graphene films, RSC Adv. 6 (2016) 106914–106920, https://doi.org/10.1039/c6ra24094a.
[43] L. Shi, S. Liu, Z. He, H. Yuan, J. Shen, Synthesis of boron and nitrogen co-doped carbon nanofiber as efficient metal-free electrocatalyst for the VO^{2+}/VO_2^+ Redox Reaction, Electrochim. Acta 178 (2015) 748–757.
[44] C. Wei, Q. Chen, C. Cheng, R. Liu, Q. Zhang, L. Zhang, Mesoporous nickel cobalt manganese sulfide yolk-shell hollow spheres for high-performance electrochemical energy storage, Inorg. Chem. Front. 6 (2019) 1851–1860, https://doi.org/10.1039/c9qi00173e.
[45] P. Thangasamy, S. Nam, S. Oh, H. Randriamahazaka, I.K. Oh, Boosting oxygen evolution reaction on metallocene-based transition metal sulfides integrated with N-doped carbon nanostructures, ChemSusChem 14 (2021) 5004–5020, https://doi.org/10.1002/cssc.202101469.
[46] D.J.H. Cant, K.L. Syres, P.J.B. Lunt, H. Radtke, J. Treacy, P.J. Thomas, E.A. Lewis, S.J. Haigh, P. Obrien, K. Schulte, F. Bondino, E. Magnano, W.R. Flavell, Surface properties of nanocrystalline PbS films deposited at the water-oil interface: a study of atmospheric aging, Langmuir 31 (2015) 1445–1453, https://doi.org/10.1021/la504779h.
[47] K. Guo, Z. Zou, J. Du, Y. Zhao, B. Zhou, C. Xu, Coupling $FeSe_2$ with CoSe: an effective strategy to create stable and efficient electrocatalysts for water oxidation, Chem. Commun. 54 (2018) 11140–11143, https://doi.org/10.1039/c8cc06628k.
[48] G.D. Park, S.J. Yang, J.H. Lee, Y.C. Kang, Investigation of binary metal (Ni, Co) selenite as Li-ion battery anode materials and their conversion reaction mechanism with Li ions, Small (2019), 1905289, https://doi.org/10.1002/smll.201905289.
[49] Z. Ali, T. Tang, X. Huang, Y. Wang, M. Asif, Y. Hou, Cobalt selenide decorated carbon spheres for excellent cycling performance of sodium ion batteries, Energy Storage Mater. 13 (2018) 19–28, https://doi.org/10.1016/j.ensm.2017.12.014.
[50] C. Wu, Y. Wei, Q. Lian, C. Cui, W. Wei, L. Chen, C. Li, Intrinsic conductivity optimization of bi-metallic nickel cobalt selenides toward superior-rate Na-ion storage, Mater. Chem. Front. 1 (2017) 2656–2663, https://doi.org/10.1039/c7qm00419b.
[51] X.L. Zhang, S.J. Hu, Y.R. Zheng, R. Wu, F.Y. Gao, P.P. Yang, Z.Z. Niu, C. Gu, X. Yu, X.S. Zheng, C. Ma, X. Zheng, J.F. Zhu, M.R. Gao, S.H. Yu, Polymorphic cobalt diselenide as extremely stable electrocatalyst in acidic media via a phase-mixing strategy, Nat. Commun. 10 (2019) 5338, https://doi.org/10.1038/s41467-019-12992-y.
[52] Z. Zheng, L. Yu, M. Gao, X. Chen, W. Zhou, C. Ma, L. Wu, J. Zhu, X. Meng, J. Hu, Y. Tu, S. Wu, J. Mao, Z. Tian, D. Deng, Boosting hydrogen evolution on MoS_2 via co-confining selenium in surface and cobalt in inner layer, Nat. Commun. 11 (2020) 3315, https://doi.org/10.1038/s41467-020-17199-0.
[53] H. Zhang, B. Yang, X. Wu, Z. Li, L. Lei, X. Zhang, Polymorphic $CoSe_2$ with mixed orthorhombic and cubic phases for highly efficient hydrogen evolution reaction, ACS Appl. Mater. Interfaces 7 (2015) 1772–1779, https://doi.org/10.1021/am507373g.
[54] M. Wang, Z. Dang, M. Prato, U. Petralanda, I. Infante, D.V. Shinde, L. De Trizio, L. Manna, Ruthenium-decorated cobalt selenide nanocrystals for hydrogen evolution, ACS Appl. Nano Mater. 2 (2019) 5695–5703, https://doi.org/10.1021/acsanm.9b01205.
[55] D. Barrera, Q. Wang, Y.J. Lee, L. Cheng, M.J. Kim, J. Kim, J.W.P. Hsu, Solution synthesis of few-layer 2H MX_2 (M = Mo, W; X = S, Se), J. Mater. Chem. C 5 (2017) 2859–2864, https://doi.org/10.1039/c6tc05097b.
[56] I. Menapace, W. Yiming, E. Masad, Effects of environmental factors on the chemical composition of asphalt binders, Energy Fuels 33 (2019) 2614–2624, https://doi.org/10.1021/acs.energyfuels.8b03273.
[57] H. Li, D. Gao, X. Cheng, Simple microwave preparation of high activity Se-rich $CoSe_2$/C for oxygen reduction reaction, Electrochim. Acta 138 (2014) 232–239, https://doi.org/10.1016/j.electacta.2014.06.065.
[58] A.K. Friedman, W. Shi, Y. Losovyj, A.R. Siedle, L.A. Baker, Mapping microscale chemical heterogeneity in Nafion membranes with X-ray photoelectron spectroscopy, J. Electrochem. Soc. 165 (2018) H733–H741, https://doi.org/10.1149/2.0771811jes.
[59] C.C. Vduva, N. Vaszilcsin, A. Kellenberger, M. Medeleanu, Catalytic enhancement of hydrogen evolution reaction on copper in the presence of benzylamine, Int. J. Hydrog. Energy 36 (2011) 6994–7001, https://doi.org/10.1016/j.ijhydene.2011.03.076.
[60] S. Anantharaj, S. Noda, M. Driess, P.W. Menezes, The pitfalls of using potentiodynamic polarization curves for tafel analysis in electrocatalytic water splitting, ACS Energy Lett. 6 (2021) 1607–1611, https://doi.org/10.1021/acsenergylett.1c00608.
[61] M.C. Lefebvre, in: B.E. Conway, J.O.'M. Bockris, R.E. White (Eds.), Modern Aspects of Electrochemistry Vol. 32, Kluwer Academic/Plenum, New York, 2002, pp. 249–300.